


Self-gravitating clusters of Fermi-Dirac gas with planar, cylindrical, or spherical symmetry: Evolution of density profiles with temperature

Michael Kirejczyk,¹ Gerhard Müller ,¹ and Pierre-Henri Chavanis²

¹*Department of Physics, University of Rhode Island, Kingston, Rhode Island 02881, USA*

²*Laboratoire de Physique Théorique, CNRS, Université Paul Sabatier, 31062 Toulouse, France*



(Received 10 October 2021; accepted 28 July 2022; published 26 August 2022)

We calculate density profiles for self-gravitating clusters of an ideal Fermi-Dirac gas with nonrelativistic energy-momentum relation and macroscopic mass at thermal equilibrium. Our study includes clusters with planar symmetry in dimensions $\mathcal{D} = 1, 2, 3$, clusters with cylindrical symmetry in $\mathcal{D} = 2, 3$, and clusters with spherical symmetry in $\mathcal{D} = 3$. Wall confinement is imposed where needed for stability against escape. The length scale and energy scale in use render all results independent of total mass and prove adequate at all temperatures. We present exact analytic expressions for (fully degenerate) $T = 0$ density profiles in four of the six combinations of symmetry and dimensionality. Our numerical results for $T > 0$ describe the emergence, upon quasistatic cooling, of a core with incipient degeneracy surrounded by a more dilute halo. The equilibrium macrostates are found to depend more strongly on the cluster symmetry than on the space dimensionality. We demonstrate the mechanical and thermal stability of spherical clusters with coexisting phases.

DOI: [10.1103/PhysRevE.106.024132](https://doi.org/10.1103/PhysRevE.106.024132)

I. INTRODUCTION

The study of self-gravitating Fermi-Dirac (FD) gases was launched in the context of white dwarf stars. Fowler [1] attributed their stability to the degenerate electron gas, whose quantum pressure arising from the Pauli exclusion principle balances the gravitational attraction at high density. Nonrelativistic white dwarfs at zero temperature represent a polytropic gas of index $n = 3/2$ [2]. Their density profile, resulting from the Lane-Emden equation [3], has a sharp surface at a finite radius. Stoner [4], Milne [5], and Chandrasekhar [6] showed that the radius r_0 of the star decreases as the mass m_{tot} increases according to the law, $m_{\text{tot}} = 91.9 \hbar^6 / (G^3 m^8 r_0^3)$ [2].

Hertel and Thirring [7,8] initiated the statistical mechanical analysis of FD clusters at nonzero temperature in the context of a study of nonrelativistic neutron stars. They found density profiles with $\sim r^{-2}$ tails, which indicates that finite-mass clusters at thermal equilibrium require artificial confinement. Moreover, Hertel and Thirring [7] proved that the mean-field assumption, which neglects correlation effects, and the Thomas-Fermi (TF) approximation, which neglects some quantum effects, are highly accurate for macroscopic systems and exact in a specific thermodynamic limit, namely $N \rightarrow +\infty$, $r_0 \rightarrow 0$, for a fixed and nonzero value of Nr_0^3 . This limit reflects the familiar mass-radius relation, $r_0 \propto N^{-1/3}$, of fully degenerate fermion stars. A different limit, $N \rightarrow \infty$, $r_0 \rightarrow \infty$ for fixed and nonzero N/r_0 , was analyzed in pioneering studies of de Vega and Sanchez [9,10]. It is the thermodynamic limit of the classical self-gravitating gas. A comparative discussion of the two limits (classical and quantum) is found in Refs. [11,12].

The exactness of the TF approximation in the thermodynamic limit can be understood by a comparison of two quantities of different origin with the same units: energy

and pressure. In a region of space with radius R and mass density ρ , the impact of the Heisenberg uncertainty principle on the quantum potential is $Q = -(\hbar^2/2m)(\Delta\sqrt{\rho}/\sqrt{\rho})$, whereas the impact of the Pauli principle on the pressure is $P = (1/20)(3/\pi)^{2/3}(h^2/m^{8/3})\rho^{5/3}$ [13]. The TF approximation assumes that the quantum potential energy density is negligible compared to the quantum pressure, $(\rho/m)Q \ll P$, which is indeed realized for $N \gg 1$. In astrophysical conditions, the TF approximation is essentially exact.

The work of Hertel and Thirring also brought forth evidence for the inequivalence of statistical ensembles in the face of long-range interactions, manifest, e.g., in negative heat capacities. This inequivalence is by no means unphysical. It locates the points of mechanical instability differently in clusters that are thermally isolated (the default in astrophysics) from clusters that are in contact with a heat bath (e.g., through the confining wall). These (spinodal) points of instability are identified in caloric curves (inverse temperature versus negative internal energy) as points of infinite slope (microcanonical ensemble) and points of zero slope (canonical ensemble).

Unlike the gravitational collapse of Maxwell-Boltzmann (MB) clusters [3,9,10,14–18], any precipitous contraction of FD clusters is arrested into a core-halo configuration by fermionic quantum statistics, which excludes multiple level occupancy. Conversely, an increase in temperature (canonical ensemble) or internal energy (microcanonical ensemble) produces an abrupt change from a core-halo configuration to flat and more spread-out density profile. The relevance of such behavior in the context of dark-matter research was investigated by Bilic and Viollier [19] in the canonical ensemble.

Chavanis [11,20] conducted an exhaustive study of phase transitions in self-gravitating FD clusters using canonical and microcanonical ensembles, confirming the results and

extending the work of Hertel and Thirring [8]. The papers [11,20] specifically identified and analyzed a zeroth-order phase transition in the microcanonical ensemble from gaseous to condensed macrostates, associated with a discontinuity in entropy. The gaseous macrostate is located at the (spinodal) stability limit. They also discussed a first-order phase transition in the microcanonical ensemble between macrostates connected by a vertical Maxwell line on the caloric curve, associated with a discontinuity in temperature. This first-order phase transition does not take place in practice on account of the fact that the lifetimes of metastable states scale exponentially with the number of particles [21].

The zeroth-order phase transition (with a discontinuity in the thermodynamic potential) has a counterpart at a different value of energy, from a condensed macrostate at the stability limit to a stable gaseous macrostate. The two transitions are complementary to each other, one representing a mechanical instability on the way down in energy (collapse) and the other on the way up (explosion). In both cases the instability precipitates processes that are associated with an increase in entropy.

A similar scenario unfolds in the canonical ensemble, but at different landmarks on the caloric curves, the control parameter being now the temperature. In particular, the zeroth-order phase transition is characterized by a discontinuity of Helmholtz free energy and the (unrealized) first-order phase transition is characterized by a discontinuity in energy associated with a horizontal Maxwell line. Interestingly, for tightly confined systems there is no phase transition, for systems with intermediate confinement a phase transition takes place in the canonical ensemble but not in the microcanonical ensemble, and for systems with loose confinement a phase transition takes place in both ensembles. This state of affairs is portrayed in intricate phase diagrams [11]. Similar results were obtained in the context of the fermionic King model [22], which does not require an artificial confinement.

Further light on the phase behavior of self-gravitating FD clusters was shed by studies that extended the space dimensionality away from $\mathcal{D} = 3$ to lower and higher values. They include Refs. [23] and [24] for properties at $T = 0$ and $T > 0$, respectively. One important insight was that $\mathcal{D} = 4$ is a sort of upper marginal dimensionality for the mechanical stability of nonrelativistic FD clusters against gravitational collapse. For $D \geq 4$, quantum mechanics cannot stabilize matter against gravitational collapse even in the nonrelativistic regime [23,24]. This is similar to a result found by Ehrenfest [25] who considered the effect of the dimension of space on the laws of physics and showed that planetary motion and the Bohr atom would not be stable in a space of dimension $D \geq 4$. A second insight was that the phase behavior exhibits features of universality across ranges of dimensionality.

In addition to white dwarf and neutron star research [26], the physics of FD clusters has applications in the study of conjectured dark matter halos made of massive neutrinos. As discussed in Refs. [22,27], the FD distribution function may be justified by the theory of violent relaxation of Lynden-Bell [28]. The statistical equilibrium state of a dark matter halo may result from a process of collisionless relaxation [28,29] rather than from a process of collisional relaxation because the relaxation time due to two-body

gravitational encounters in dark matter halos is much larger than the age of the universe. However, the collisional relaxation time may be reduced if the fermions are self-interacting [27]. The equilibrium states generically have a core-halo structure made of a quantum core (fermion ball) surrounded by an isothermal halo (envelope) [27,30].

Some authors [31–34] have proposed that a very compact quantum core made of dark matter fermions with mass $\sim 50 \text{ keV}/c^2$ could mimic a supermassive black hole at the center of the galaxies. Other authors [22,27,35] have considered a smaller fermion mass of $\sim 1 \text{ keV}/c^2$ and argued that the quantum core has the shape of a large dark matter bulge. It is also possible that sufficiently large fermionic dark matter halos are nondegenerate [36]. We refer to Ref. [27] for a comparison between these different scenarios. The nature of dark matter, let alone the values of relevant particle masses, are very much in dispute.

This work, which emphasizes the distinction between cluster symmetry and space dimensionality, begins with establishing the conditions of mechanical stability and thermal equilibrium (Sec. II). A second point of emphasis is the choice of practical scales for length and energy (Sec. III). In the discussion of fully degenerate finite-mass clusters the emphasis is on exact results for density profiles (Sec. IV). The centerpieces for the analysis and interpretation of FD clusters at $T > 0$ are robust free-energy expressions and caloric curves (Sec. V). With these tools in place, we are ready to analyze density profiles subject to gradual and abrupt changes upon cooling or heating (Sec. VI) and to describe phase-coexisting macrostates (Sec. VII).

II. EQUILIBRIUM CONDITIONS

The density profiles of self-gravitating FD gas clusters analyzed in this work are governed by mechanical stability and thermal equilibrium. The former is encoded in an equation of motion (EOM) and the latter in an equation of state (EOS). In the present context, mechanical stability means hydrostatic equilibrium. The only particle interaction included is the mutual gravitational attraction. The mean-field assumption is validated by the long range nature of this force [7].

We consider clusters with planar symmetry ($\mathcal{D}_\sigma = 1$), cylindrical symmetry ($\mathcal{D}_\sigma = 2$), and spherical symmetry ($\mathcal{D}_\sigma = 3$). All profiles are functions of the distance r from the center of the cluster. For $\mathcal{D}_\sigma = 1$, the center is a point, a line, or a plane in $\mathcal{D} = 1, 2, 3$, respectively. For $\mathcal{D}_\sigma = 2$, the center is a point or a line in $\mathcal{D} = 2, 3$, respectively. For $\mathcal{D}_\sigma = 3$, the center is a point (in $\mathcal{D} = 3$). We thus write $\rho_v(r)$ and $p(r)$ for the radial profiles of particle density and pressure, respectively. The temperature T is uniform.

The total number of particles in a finite cluster is obtained from the density profile via the integral,

$$N = L^{\mathcal{D}-\mathcal{D}_\sigma} \int_0^R dr \mathcal{A}_{\mathcal{D}_\sigma} r^{\mathcal{D}_\sigma-1} \rho_v(r), \quad (1)$$

where R is the radius of the confining wall, L the length of a cylinder or of the sides of a plane in cases with $\mathcal{D}_\sigma < \mathcal{D}$, and $\mathcal{A}_{\mathcal{D}} \doteq 2\pi^{\mathcal{D}/2}/\Gamma(\mathcal{D}/2)$ is the surface area of the \mathcal{D} -dimensional unit sphere. The condition $L \gg R$ guarantees that deviations from the symmetry assumed to hold are negligible.

Hydrostatic equilibrium relates pressure and density,

$$\frac{d}{dr}p(r) = M\rho_v(r)g(r), \quad (2)$$

involving the gravitational field,

$$g(r) = -\frac{\mathcal{A}_{\mathcal{D}}G_{\mathcal{D}}M}{r^{\mathcal{D}_\sigma-1}} \int_0^r dr' r'^{\mathcal{D}_\sigma-1} \rho_v(r'). \quad (3)$$

To accommodate scenarios which include plasmas, we distinguish the kinetic mass m (e.g., of electrons) entering the EOS and the gravitational mass M (e.g., of nucleons per electron) entering the EOM. The total mass of a cluster is denoted m_{tot} . The strength $G_{\mathcal{D}}$ of the gravitational interaction is empirically known, of course, only in $\mathcal{D} = 3$.

The EOS (in the local density approximation) for a nonrelativistic FD gas in \mathcal{D} dimensions is implicit in the relations,

$$\rho_v(r)\lambda_T^{\mathcal{D}} = g_s f_{\mathcal{D}/2}[z(r)], \quad (4a)$$

$$u_v(r)\lambda_T^{\mathcal{D}} = \frac{\mathcal{D}}{2}k_B T g_s f_{\mathcal{D}/2+1}[z(r)], \quad (4b)$$

$$\frac{p'(r)\lambda_T^{\mathcal{D}}}{k_B T} = g_s \frac{d}{dz} f_{\mathcal{D}/2+1}(z)z'(r), \quad (4c)$$

between the particle density, the kinetic energy density, and the pressure, parametrized by the fugacity profile $z(r)$. Here g_s is the spin degeneracy, $\lambda_T = \sqrt{\hbar^2/2\pi m k_B T}$ is the de Broglie thermal wavelength, and

$$f_n(z) \doteq \frac{1}{\Gamma(n)} \int_0^\infty \frac{dx x^{n-1}}{z^{-1}e^x + 1} = \sum_{l=1}^{\infty} (-1)^{l-1} \frac{z^l}{l^n}, \quad z \geq 0 \quad (5)$$

are the (polylogarithmic) FD functions with the familiar special cases, $f_0(z) = z/(1+z)$, $f_1(z) = \ln(1+z)$, and $f_\infty(z) = z$. The entropy density,

$$\frac{s\lambda_T^{\mathcal{D}}}{g_s k_B} = \left(\frac{\mathcal{D}}{2} + 1\right) f_{\mathcal{D}/2+1}(z) - \ln z f_{\mathcal{D}/2}(z) \quad (6)$$

is inferred from Eq. (4) via Euler's equation, $u_v = Ts - p - \mu\rho_v$ with $\mu = k_B T \ln z$.

We have rendered Eq. (4c) in a way that consistency with Eq. (2) is ensured even under phase coexistence. Substitution of Eq. (4c) into Eq. (2) with use of Eq. (3) and the recurrence relation $z f_n'(z) = f_{n-1}(z)$ produces the ODE,

$$\frac{z''}{z} + \frac{\mathcal{D}_\sigma - 1}{r} \frac{z'}{z} - \left(\frac{z'}{z}\right)^2 + \frac{g_s \mathcal{A}_{\mathcal{D}} G_{\mathcal{D}} M^2}{\lambda_T^{\mathcal{D}} k_B T} f_{\mathcal{D}/2}(z) = 0, \quad (7)$$

for the fugacity profile, from which the density profile follows via Eq. (4a).

For (thermodynamically) open systems, which include clusters of finite and infinite mass, the boundary conditions are

$$z'(0) = 0, \quad 0 < z(0) = z_0, \quad (8)$$

with the (average) total mass, $m_{\text{tot}} = NM$, provided it is finite, inferred from Eq. (1). Closed systems of finite mass may only exist under confinement such as imposed by a wall at $R < \infty$. For cases with $\mathcal{D}_\sigma < \mathcal{D}$, it is useful to introduce a rescaled

number of particles:

$$\tilde{N} \doteq \frac{N}{L^{\mathcal{D}-\mathcal{D}_\sigma}}. \quad (9)$$

The second boundary condition Eq. (8) is to be replaced (for closed systems) by the integral (1) converted into

$$\frac{g_s \mathcal{A}_{\mathcal{D}_\sigma}}{\tilde{N} \lambda_T^{\mathcal{D}}} \int_0^R dr r^{\mathcal{D}_\sigma-1} f_{\mathcal{D}/2}(z) = 1. \quad (10)$$

III. SCALING CONVENTION

For our analysis we have constructed a length scale and an energy scale that are useful for the description of macroscopic FD clusters at all temperatures including $T = 0$. These scales work equally well for the gaseous part of Bose-Einstein (BE) clusters [37]. The length scale r_s and temperature scale T_s are derived from the thermal wavelength and a macroscopic reference volume as follows:

$$\hat{r} \doteq \frac{r}{r_s}, \quad \hat{T} \doteq \frac{T}{T_s}, \quad (11)$$

$$\tilde{N} \lambda_{T_s}^{\mathcal{D}} = \frac{\mathcal{A}_{\mathcal{D}_\sigma}}{\mathcal{D}_\sigma} r_s^{\mathcal{D}_\sigma}, \quad \frac{1}{r_s^2} = \frac{1}{2\mathcal{D}_\sigma} \frac{\mathcal{A}_{\mathcal{D}} G_{\mathcal{D}} M^2}{\lambda_{T_s}^{\mathcal{D}} k_B T_s}. \quad (12)$$

The first Eq. (12) divides the hypersphere of radius r_s into \tilde{N} hypercubes of side λ_{T_s} . The second Eq. (12) relates the coefficient in the last term of Eq. (7), which must be an inverse squared length, with r_s . Relations (12) determine r_s and T_s as functions of particle mass m and total mass $m_{\text{tot}} = NM$ for cases with $\mathcal{D}_\sigma = \mathcal{D}$ (see Appendix A). If $\mathcal{D}_\sigma < \mathcal{D}$, then we use $\tilde{m}_{\text{tot}} = \tilde{N}M$ with \tilde{N} from Eq. (9) instead, which can still be used as a measure for how massive the cluster is.

Expressed in the dimensionless variables thus defined, including the relation $\hat{z}(\hat{r}) \doteq z(r)$, the ODE (7) becomes

$$\frac{\hat{z}''}{\hat{z}} + \frac{\mathcal{D}_\sigma - 1}{\hat{r}} \frac{\hat{z}'}{\hat{z}} - \left(\frac{\hat{z}'}{\hat{z}}\right)^2 + \frac{2\mathcal{D}_\sigma}{\hat{T}} \rho(\hat{r}) = 0, \quad (13)$$

where we use the dimensionless density,

$$\rho(\hat{r}) \doteq \lambda_{T_s}^{\mathcal{D}} \rho_v(\hat{r}) = g_s \hat{T}^{\mathcal{D}/2} f_{\mathcal{D}/2}(\hat{z}), \quad (14)$$

and rewrite Eq. (10) in the form

$$\mathcal{D}_\sigma \int_0^{\hat{R}} d\hat{r} \hat{r}^{\mathcal{D}_\sigma-1} \rho(\hat{r}) = 1. \quad (15)$$

Contact with a frequently used alternative scaling convention, whose advantage is to demonstrate the classical limit, is established in Appendix A.

IV. DEGENERATE CLUSTERS

FD clusters of finite mass at zero temperature are stable against particle escape. They are also stable against gravitational collapse for $1 \leq \mathcal{D}_\sigma \leq \mathcal{D} \leq 3$ as long as the total mass does not push the Fermi momentum into the relativistic regime. Density profiles of fully degenerate FD clusters are important anchor points for the analysis of the effects of rising temperature (Sec. VI). Relativistic effects in temperature and mass variations will be investigated elsewhere [38].

For the purpose of investigating $T = 0$ density profiles, we distill out of the ODE (7) for the fugacity $z(r)$ an ODE for the chemical potential $\mu(r) = k_B T \ln z(r)$ in the limit $T \rightarrow 0$, using the leading term in the asymptotic expansion of FD functions,

$$f_{\mathcal{D}/2}(z) \rightsquigarrow \frac{(\beta\mu)^{\mathcal{D}/2}}{\Gamma(\mathcal{D}/2 + 1)}. \quad (16)$$

The ODE for the chemical potential, expressed in scaled variables, $\hat{\mu} \doteq \mu/k_B T_s$ and $\hat{r} \doteq r/r_s$, which for $\mathcal{D}_\sigma = \mathcal{D}$ has the structure of a Lane-Emden equation, reads

$$\hat{\mu}'' + \frac{\mathcal{D}_\sigma - 1}{\hat{r}} \hat{\mu}' + \frac{2g_s \mathcal{D}_\sigma}{\Gamma(\mathcal{D}/2 + 1)} \hat{\mu}^{\mathcal{D}/2} = 0. \quad (17)$$

We are seeking a solution with boundary conditions,

$$\hat{\mu}'(0) = 0, \quad \hat{\mu}(\hat{r}_0) = 0, \quad (18)$$

where the cluster radius \hat{r}_0 is implicitly determined by the normalization condition (15) adapted as follows:

$$\frac{g_s \mathcal{D}_\sigma}{\Gamma(\mathcal{D}/2 + 1)} \int_0^{\hat{r}_0} d\hat{r} \hat{r}^{\mathcal{D}_\sigma - 1} [\hat{\mu}(\hat{r})]^{\mathcal{D}/2} = 1. \quad (19)$$

The tacit assumption is that $\hat{R} > \hat{r}_0$. Fully degenerate FD clusters are self-confined.

The (scaled) density and pressure profiles, expressed via chemical potential, inferred from Eqs. (4) and the asymptotics (16), become

$$\rho(\hat{r}) = \frac{g_s [\hat{\mu}(\hat{r})]^{\mathcal{D}/2}}{\Gamma(\mathcal{D}/2 + 1)} \theta(\hat{r}_0 - \hat{r}), \quad (20)$$

$$\hat{p}(\hat{r}) \doteq \frac{p(r)}{k_B T_s \lambda_{T_s}^{-\mathcal{D}}} = \frac{g_s [\hat{\mu}(\hat{r})]^{\mathcal{D}/2 + 1}}{\Gamma(\mathcal{D}/2 + 2)} \theta(\hat{r}_0 - \hat{r}), \quad (21)$$

which confirms the result of Ref. [23] that we are dealing with polytropes of index $n = \mathcal{D}/2$, independent of \mathcal{D}_σ (see Appendix C for more details). The linear cusp of $\hat{\mu}(\hat{r})$ at \hat{r}_0 determines the power-law cusp singularities of the density $\rho(\hat{r})$ and the pressure $\hat{p}(\hat{r})$ at the surface of the cluster via Eqs. (20) and (21).

In the following we analyze the solutions of Eqs. (17)–(19) separately for the six combinations $0 \leq \mathcal{D}_\sigma \leq \mathcal{D} \leq 3$. Within the nonrelativistic regime, all scaled profiles are universal, i.e., independent of total mass.

A. $\mathcal{D}_\sigma = \mathcal{D} = 1$

The ODE (17) for the scaled chemical potential $\hat{\mu}(\hat{r})$ simplifies into

$$\hat{\mu}'' + \frac{2g_s}{\Gamma(3/2)} \hat{\mu}^{1/2} = 0. \quad (22)$$

We solve it by transcribing it to

$$\hat{r}'' - \frac{2g_s}{\Gamma(3/2)} \sqrt{\hat{\mu}} [\hat{r}']^3 = 0, \quad (23)$$

for the inverse function $\hat{r}(\hat{\mu})$, thus reducing it effectively to first order (see Ref. [39] for a different approach). The first integral is carried out by separation of the variables $\hat{\mu}$ and

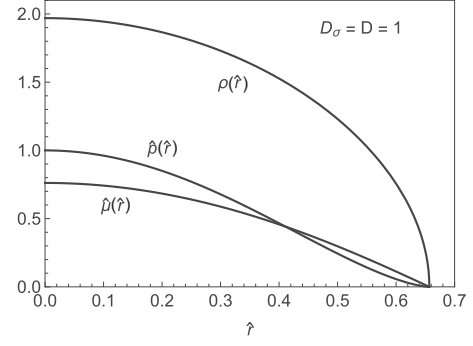


FIG. 1. Universal profiles for the scaled chemical potential, density, and pressure of the nonrelativistic FD gas with $\mathcal{D}_\sigma = \mathcal{D} = 1$ at $T = 0$.

$\hat{s} \doteq \hat{r}'(\hat{\mu})$ with use of the boundary condition, $\hat{r}'(\hat{\mu}_0) = -\infty$:

$$\int_{-\infty}^{\hat{s}} \frac{d\hat{s}'}{\hat{s}'^3} = \frac{2g_s}{\Gamma(3/2)} \int_{\hat{\mu}_0}^{\hat{\mu}} d\hat{\mu}' \sqrt{\hat{\mu}'}. \quad (24)$$

We thus obtain

$$\hat{r}'(\hat{\mu}) = - \left(\frac{3\Gamma(3/2)}{8g_s} \right)^{1/2} \sqrt{\frac{1}{\hat{\mu}_0^{3/2} - \hat{\mu}^{3/2}}}. \quad (25)$$

The inverse profile then reads

$$\hat{r}(\hat{\mu}) = \hat{r}_0 - \left(\frac{3\Gamma(3/2)}{8g_s} \right)^{1/2} \int_0^{\hat{\mu}} \frac{d\hat{\mu}'}{\sqrt{\hat{\mu}_0^{3/2} - \hat{\mu}'^{3/2}}}, \quad (26)$$

for $0 \leq \hat{\mu} \leq \hat{\mu}_0$. Implementing $\hat{r}(\hat{\mu}_0) = 0$ from Eq. (18) yields

$$\hat{r}_0 = \left(\frac{3\Gamma(3/2)}{8g_s} \right)^{1/2} \hat{\mu}_0^{1/4} \int_0^1 \frac{dx}{\sqrt{1 - x^{3/2}}} \quad (27)$$

$$= \frac{1}{4} \sqrt{\frac{3\pi^{3/2}}{g_s}} \frac{\Gamma(5/3)}{\Gamma(7/6)} \hat{\mu}_0^{1/4}. \quad (28)$$

Condition (19) is satisfied by the values $\hat{\mu}_0 = 0.76162$ and $\hat{r}_0 = 0.656793$ if we set $g_s = 2$.

In Fig. 1 we plot the profile for the chemical potential derived from the solution (26) and the profiles (20) and (21) for density and pressure, respectively. The function $\hat{\mu}(\hat{r})$ vanishes linearly at $\hat{r} = \hat{r}_0$ (to leading order), implying cusp singularities, $\rho \sim (\hat{r}_0 - \hat{r})^{1/2}$ and $\hat{p} \sim (\hat{r}_0 - \hat{r})^{3/2}$ for the other two functions. When particles are added, the radius of the cluster increases at the rate $r_0 \sim N^{1/3}$ and the pressure at the center of the cluster increases at the rate $p(0) \sim N^2$.

B. $\mathcal{D}_\sigma = 1, \mathcal{D} = 2$

For this case the ODE (17) becomes linear,

$$\hat{\mu}'' + 2g_s \hat{\mu} = 0, \quad (29)$$

and the solution for $g_s = 2$ which satisfies the boundary conditions (18) and (19) takes the form

$$\hat{\mu}(\hat{r}) = \cos(2\hat{r}), \quad (30)$$

implying $\hat{r}_0 = \pi/4$ and $\hat{\mu}_0 = 1$. This profile along with the profiles (20) and (21) are shown in Fig. 2.

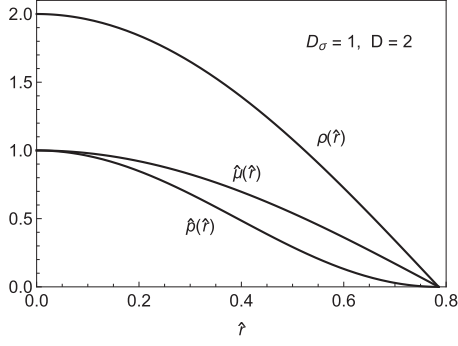


FIG. 2. Universal profiles for the scaled chemical potential, density, and pressure of the nonrelativistic FD gas with $\mathcal{D}_\sigma = 1$, $\mathcal{D} = 2$ at $T = 0$.

The chemical potential and the density have proportional profiles, approaching zero linearly at \hat{r}_0 , whereas the pressure vanishes quadratically at the surface of the cluster. Adding particles does not change the radius of the cluster. In consequence, the local density grows linearly with mass. The central pressure increases quadratically with mass.

C. $\mathcal{D}_\sigma = 1$, $\mathcal{D} = 3$

The ODE to be solved in this case is

$$\hat{\mu}'' + \frac{2g_s}{\Gamma(5/2)}\hat{\mu}^{3/2} = 0 \quad (31)$$

for the function $\hat{\mu}(\hat{r})$ or the (effectively first-order) ODE,

$$\hat{r}'' - \frac{2g_s}{\Gamma(5/2)}\hat{\mu}^{3/2}[\hat{r}']^3 = 0, \quad (32)$$

for the inverse function $\hat{r}(\hat{\mu})$. The resulting inverse profile becomes

$$\hat{r}(\hat{\mu}) = \hat{r}_0 - \left(\frac{5\Gamma(5/2)}{8g_s}\right)^{1/2} \int_0^{\hat{\mu}} \frac{d\hat{\mu}'}{\sqrt{\hat{\mu}_0^{5/2} - \hat{\mu}'^{5/2}}}, \quad (33)$$

for $0 \leq \hat{\mu} \leq \hat{\mu}_0$. Implementing conditions (18) and (19) yields the relation

$$\begin{aligned} \hat{r}_0 &= \left(\frac{5\Gamma(5/2)}{8g_s}\right)^{1/2} \hat{\mu}_0^{-1/4} \int_0^1 \frac{dx}{\sqrt{1-x^{5/2}}} \\ &= \frac{1}{4} \sqrt{\frac{15\pi^{3/2}}{2g_s}} \frac{\Gamma(7/5)}{\Gamma(9/10)} \hat{\mu}_0^{-1/4}, \end{aligned} \quad (34)$$

and the values $\hat{\mu}_0 = 1.225233$, $\hat{r}_0 = 0.901549$. The profiles (20) and (21) follow directly (see Fig. 3).

The linear cusp of the chemical potential at \hat{r}_0 is universal in $\mathcal{D}_\sigma = 1$. The cusp singularities of density and pressure become weaker as \mathcal{D} increases. The (unscaled) radius r_0 shrinks with increasing mass: $r_0 \sim N^{-1/5}$.

D. $\mathcal{D}_\sigma = \mathcal{D} = 2$

The term with a first-order derivative in the ODE (17) for $\mathcal{D}_\sigma > 1$ removes the advantage of switching to inverse functions. However, for $\mathcal{D} = 2$, the ODE

$$\hat{\mu}'' + \frac{1}{\hat{r}}\hat{\mu}' + 4g_s\hat{\mu} = 0 \quad (35)$$

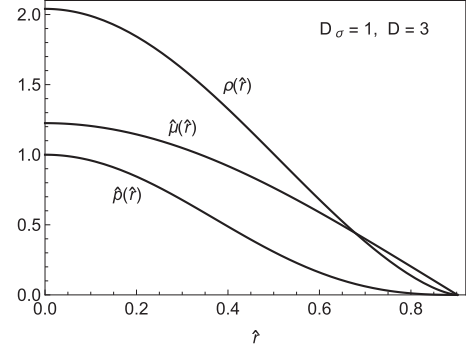


FIG. 3. Universal profiles for the scaled chemical potential, density, and pressure of the nonrelativistic FD gas with $\mathcal{D}_\sigma = 1$, $\mathcal{D} = 3$ at $T = 0$.

is recognizable as characteristic of Bessel functions. The solution which satisfies the boundary conditions (18) and (19) with $g_s = 2$ is well known [23]:

$$\hat{\mu}(\hat{r}) = \hat{\mu}_0 J_0(2\sqrt{2}\hat{r}). \quad (36)$$

The radius \hat{r}_0 of the cluster is determined by the first zero of the Bessel function. The value $\hat{\mu}_0$ then follows from Eq. (19). We thus obtain $\hat{\mu}_0 = 1.60198$ and $\hat{r}_0 = 0.850234$. The profile (36) along with the profiles (20) and (21) are shown in Fig. 4.

The chemical potential and the density are directly proportional and vanish linearly at the edge of the cluster whereas the pressure vanishes quadratically. Features shared by all cases with $\mathcal{D} = 2$ include that the average density and total mass are proportional, the radius of the cluster is independent of the mass, and the central pressure increases quadratically with mass.

E. $\mathcal{D}_\sigma = 2$, $\mathcal{D} = 3$

This case requires that we numerically solve the ODE

$$\hat{\mu}'' + \frac{1}{\hat{r}}\hat{\mu}' + \frac{4g_s}{\Gamma(5/2)}\hat{\mu}^{3/2} = 0, \quad (37)$$

subject to the simultaneous conditions (18) and (19). The solution is unique and has the values, $\hat{\mu}_0 = 1.88488$, for the central chemical potential and, $\hat{r}_0 = 0.92098$, for the cluster

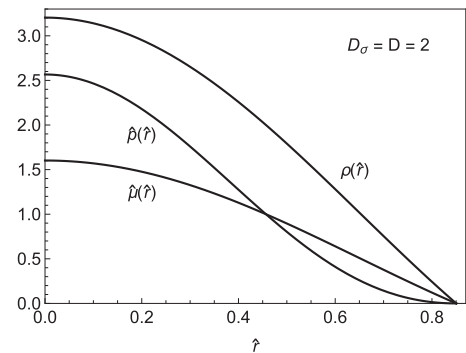


FIG. 4. Universal profiles for the scaled chemical potential, density, and pressure of the nonrelativistic FD gas with $\mathcal{D}_\sigma = \mathcal{D} = 2$ at $T = 0$.

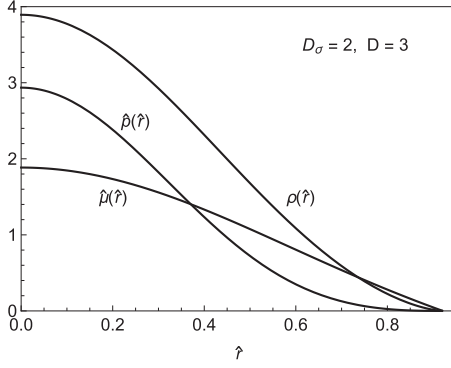


FIG. 5. Universal profiles for the scaled chemical potential, density, and pressure of the nonrelativistic FD gas with $\mathcal{D}_\sigma = 2$, $\mathcal{D} = 3$, at $T = 0$.

radius. The solution $\hat{\mu}(\hat{r})$ of Eq. (37) and the profiles of $\rho(\hat{r})$, $\hat{p}(\hat{r})$ inferred from Eqs. (20) and (21) are shown in Fig. 5.

F. $\mathcal{D}_\sigma = 3$, $\mathcal{D} = 3$

The universal profiles for this case are of textbook familiarity [2]. The analysis of

$$\hat{\mu}'' + \frac{2}{\hat{r}}\hat{\mu}' + \frac{6g_s}{\Gamma(5/2)}\hat{\mu}^{3/2} = 0 \quad (38)$$

must again be carried out numerically in its entirety. The specifications of the solution which satisfies the three conditions (18) and (19) are $\hat{\mu}_0 = 2.88587$ and $\hat{r}_0 = 0.932973$. The resulting profiles of $\hat{\mu}(\hat{r})$, $\rho(\hat{r})$, and $\hat{p}(\hat{r})$ are shown in Fig. 6. While the radius shrinks in real space when particles are added, $r_0 \sim N^{-1/3}$, it grows in reciprocal space, $\mu_0 \sim N^{4/3}$. The central pressure rises rapidly with increasing mass: $p(0) \sim N^{10/3}$.

G. Mass-radius relation

Our choice of length scale has the advantage of producing universal profiles. Clusters of given symmetry and dimensionality have their surface at a specific numerical value of the scaled radius \hat{r}_0 irrespective of mass (within the nonrelativistic regime). In consequence, the mass-radius relation of

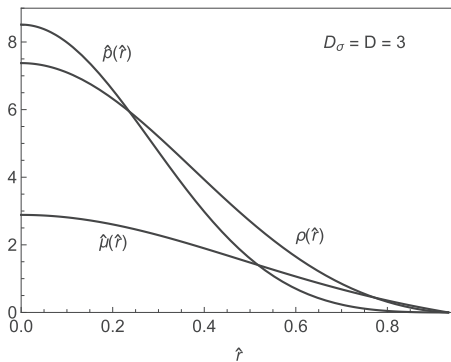


FIG. 6. Universal profiles for the scaled chemical potential, density, and pressure of the nonrelativistic FD gas in $\mathcal{D}_\sigma = \mathcal{D} = 3$ at $T = 0$.

TABLE I. Explicit dependence of the length scale r_s , which determines the cluster radius at $T = 0$ via $r_0 = \hat{r}_0 r_s$ on the number N of particles with (kinetic) mass m and (gravitational) mass M . The total mass is $m_{\text{tot}} = NM$. For cases with $\mathcal{D}_\sigma < \mathcal{D}$ we use \tilde{N} as defined in Eq. (9). The six relations are extracted from Eq. (12).

\mathcal{D}_σ	\mathcal{D}	r_s
1	1	$\left(\frac{\pi\hbar^2}{G_1}\right)^{1/3} \frac{N^{1/3}}{M^{2/3}m^{1/3}}$
1	2	$\hbar\sqrt{\frac{2}{G_2}}M^{-1}m^{-1/2}$
1	3	$\left(\frac{2\hbar^6}{G_3^3}\right)^{1/5} \tilde{N}^{-1/5}M^{-6/5}m^{-3/5}$
2	2	$\frac{2\hbar}{\sqrt{G_2}}M^{-1}m^{-1/2}$
2	3	$\left(\frac{8\pi\hbar^6}{G_3^3}\right)^{1/4} \tilde{N}^{-1/4}M^{-3/2}m^{-3/4}$
3	3	$(36\pi)^{1/3} \frac{\hbar^2}{G_3} \tilde{N}^{-1/3}M^{-2}m^{-1}$

self-gravitating clusters—a quantity of considerable interest—is encoded in the length scale r_s .

In Table I we state the explicit dependence of r_s on the number of particles N , and on the relevant kinetic mass m and gravitational mass M of particles. The total mass is $m_{\text{tot}} = NM$. In ordinary matter m is the electron mass and M the mass of nucleons per electron.

The relations compiled in Table I, at least the entries for $\mathcal{D} = 3$, are likely to be of importance in dark matter research, where it is still unclear what particle mass M might dominate gravity and what particle mass m might dominate the pressure (via the thermal wavelength). The distinct dependencies of the cluster radius on the two particle masses is potentially useful for providing clues about the range of particle masses that qualify as constituents of dark matter.

V. FREE ENERGIES AND CALORIC CURVES

For the analysis of density profiles at $T > 0$ it is useful to have caloric curves—functional relations between inverse scaled temperature and negative scaled internal energy—available as a road map on which relevant landmarks can be identified, namely points of instability in both the canonical and microcanonical ensembles. Caloric curves were analyzed in Ref. [24] for $\mathcal{D} = \mathcal{D}_\sigma$ using a different scaling convention (Appendix A).

In the following, we present caloric curves and use them as a guide for the interpretation of how $T > 0$ density profiles evolve between the MB limit and the fully degenerate state. Another diagnostic tool for the same purpose in the canonical ensemble is the Helmholtz free energy:

$$F = E - TS = U + W - TS, \quad (39)$$

where U is the kinetic energy, $E = U + W$ the internal energy, S the entropy, and W the (gravitational) potential energy. In the microcanonical ensemble, the role of thermodynamic potential is taken over by the entropy S .

A. Kinetic energy and entropy

From the expressions developed earlier we infer the following integrals for the kinetic energy and the entropy:

$$\hat{U} \doteq \frac{U}{Nk_B T_s} = \mathcal{D}_\sigma g_s \hat{T}^{\mathcal{D}/2+1} \frac{\mathcal{D}}{2} \int_0^{\hat{R}} d\hat{r} \hat{r}^{\mathcal{D}_\sigma-1} f_{\mathcal{D}/2+1}(\hat{z}), \quad (40)$$

$$\begin{aligned} \hat{S} \doteq \frac{S}{Nk_B} &= \mathcal{D}_\sigma g_s \hat{T}^{\mathcal{D}/2} \int_0^{\hat{R}} d\hat{r} \hat{r}^{\mathcal{D}_\sigma-1} \\ &\times \left[\left(\frac{\mathcal{D}}{2} + 1 \right) f_{\mathcal{D}/2+1}(\hat{z}) - \ln \hat{z} f_{\mathcal{D}/2}(\hat{z}) \right], \quad (41) \end{aligned}$$

implying

$$\begin{aligned} \hat{U} - \hat{T} \hat{S} &= -\mathcal{D}_\sigma g_s \hat{T}^{\mathcal{D}/2+1} \int_0^{\hat{R}} d\hat{r} \hat{r}^{\mathcal{D}_\sigma-1} \\ &\times [f_{\mathcal{D}/2+1}(\hat{z}) - \ln \hat{z} f_{\mathcal{D}/2}(\hat{z})]. \quad (42) \end{aligned}$$

B. Potential energy

The construction of the potential energy W for self-gravitating clusters requires some thought. In all cases $1 \leq \mathcal{D}_\sigma \leq \mathcal{D} \leq 3$ we choose a reference state (pseudo-vacuum) different from the ground state (physical vacuum), namely the state with all particles confined to $0 \leq r \leq r_c$ at uniform density in real space. All differences ΔW between macrostates are independent of r_c .

We calculate the differential dW as work performed against gravity when a thin layer of mass is translocated from the reference density profile to the actual density profile, a method developed in the context of a self-gravitating lattice gas [40]. This construction turns out to be also useful for BE clusters [37]. Alternative expressions for W , which are equivalent and derived from the virial theorem, can be found in Appendix B.

For FD clusters with planar symmetry ($\mathcal{D}_\sigma = 1$) we arrive at the expression,

$$\begin{aligned} \hat{W} \doteq \frac{W}{Nk_B T_s} &= 2 \int_0^{\hat{R}} d\hat{r}_2 \hat{r}_2 \sigma_1(\hat{r}_2) \rho(\hat{r}_2) - \frac{2}{3} \hat{r}_c, \\ \sigma_1(\hat{r}_2) \doteq \int_0^{\hat{r}_2} d\hat{r} \hat{r} \rho(\hat{r}) &= -\frac{\hat{T}}{2} \frac{\hat{z}'(\hat{r})}{\hat{z}(\hat{r})}. \quad (43) \end{aligned}$$

The corresponding expression for clusters with cylindrical symmetry ($\mathcal{D}_\sigma = 2$) has a quite different look:

$$\begin{aligned} \hat{W} &= 4 \int_0^{\hat{R}} d\hat{r}_2 \hat{r}_2 \sigma_2(\hat{r}_2) \rho(\hat{r}_2) \ln \left(\frac{\hat{r}_2}{\sqrt{\sigma_2(\hat{r}_2)}} \right) - \ln \hat{r}_c, \\ \sigma_2(\hat{r}_2) \doteq 2 \int_0^{\hat{r}_2} d\hat{r} \hat{r} \rho(\hat{r}) &= -\frac{\hat{T}}{2} \hat{r}^2 \frac{\hat{z}'(\hat{r})}{\hat{z}(\hat{r})}. \quad (44) \end{aligned}$$

The logarithmic terms, characteristic for cylindrical symmetry, disappear for spherical symmetry ($\mathcal{D}_\sigma = 3$):

$$\begin{aligned} \hat{W} &= -6 \int_0^{\hat{R}} d\hat{r}_2 \hat{r}_2 \sigma_3(\hat{r}_2) \rho(\hat{r}_2) + \frac{6}{5} \hat{r}_c^{-1}, \\ \sigma_3(\hat{r}_2) \doteq 3 \int_0^{\hat{r}_2} d\hat{r} \hat{r}^2 \rho(\hat{r}) &= -\frac{\hat{T}}{2} \hat{r}^2 \frac{\hat{z}'(\hat{r})}{\hat{z}(\hat{r})}. \quad (45) \end{aligned}$$

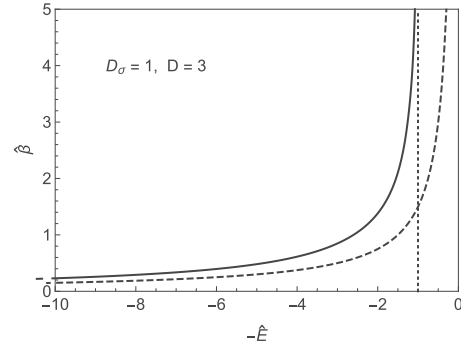


FIG. 7. Caloric curves for the FD cluster (solid line) and MB cluster (dashed line) with planar symmetry and $\hat{R} = \infty$ in three-dimensional space. The dotted line marks the energy of the fully degenerate cluster identified in Sec. IV C. The MB result reflects the internal energy $E = \frac{5}{2} Nk_B T$ (see Appendix B).

The dependence on \mathcal{D} in all cases is contained in the profiles $\hat{z}(\hat{r})$ and $\rho(\hat{r})$.

C. Caloric curves

An examination of caloric curves sets the stage for the analysis of $T > 0$ density profiles in Sec. VI. Our scaling convention suggests that we plot $\hat{\beta} \doteq k_B T_s / k_B T$ versus $\hat{E} \doteq E / Nk_B T_s$. The scaled radius of confinement $\hat{R} \doteq R / r_s$ is a useful parameter. A more detailed discussion of caloric curves can be found in Refs. [11,24]. In Appendix A we explain the different scaling conventions in use. In the following, we highlight systems for $\mathcal{D}_\sigma = 1, 2, 3$ in $\mathcal{D} = 3$. The symmetry of the cluster has a stronger impact on caloric curves than the dimensionality of the space.

Caloric curves of clusters with planar symmetry are monotonically increasing across the complete range of inverse temperature (see Fig. 7). The range of negative internal energy has no lower limit, but reaches an upper limit, at $\hat{E}_{\min} = \frac{10}{9} \hat{r}_0$, where $\hat{r}_0 = 0.9015 \dots$ is the radius of the self-confined cluster identified in Sec. IV C.

The featureless structure of these caloric curves predicts that the cooling of FD clusters with planar symmetry incites a very gradual response throughout. The cooling of MB clusters with planar symmetry is equally uneventful. The FD caloric curves deviate from the MB caloric curve as the exclusion principle comes into play. Effects of wall confinement (not shown) are significant only when the space is very tight or the temperature very high (for confined systems, $E \sim \frac{\mathcal{D}}{2} Nk_B T$ when $T \rightarrow +\infty$).

The caloric curves for FD clusters with cylindrical symmetry are still strictly monotonic as shown in Fig. 8(a), but they are no longer featureless. There is a plateau in the vicinity of the characteristic temperature $\hat{T}_{\text{MB}} = \frac{1}{2}$, where the MB cluster is known to undergo a gravitational collapse as evident in Fig. 8(b). Here the plateau reaches all the way to $\hat{E} \rightarrow -\infty$, where the MB cluster has contracted to a point.

The FD caloric curves with the plateau feature represent a phenomenon of incipient gravitational collapse, more or less gently arrested by the counteracting exclusion pressure. However, there is no hint of gravitational collapse if the aver-

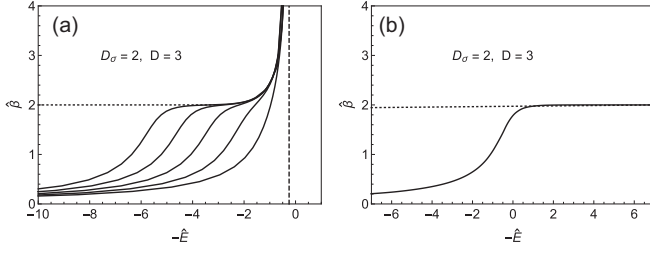


FIG. 8. (a) Caloric curves for FD clusters with confining radius $\hat{R} = 1.50, 4.70, 14.9, 47.0, 149$ (right to left) and $\hat{R} = \infty$ (dotted line). The dashed lines mark the energy of the fully degenerate FD cluster identified in Sec. IV E. (b) Caloric curve for MB clusters of any \hat{R} . The dotted line marks temperature $\hat{T}_{\text{MB}} = \frac{1}{2}$ at which the MB clusters collapse.

age interparticle distance is comparable to thermal wavelength already at temperatures near \hat{T}_{MB} . This is the case under tight confinement. In summary, despite the added structure, the strict monotonicity of all FD caloric curves for clusters with cylindrical symmetry rules out any mechanical instabilities or phase transitions.

A whole new level of drama is on display in the caloric curves for FD clusters with spherical symmetry (Fig. 9). Here we see everything that we already identified and much more. In very tight quarters ($\hat{R} \ll 1$), the caloric curve is monotonic and featureless as is the case universally in planar clusters. As we relax the confinement by increasing \hat{R} , a shoulder makes its appearance, which is reminiscent of caloric curves of cylindrical clusters.

Upon further widening of the space to which the FD gas is confined, hitherto unseen structures emerge. The first novel structural feature that makes its appearance is local maximum followed by a local minimum, two points with zero slope. They signal the presence of multiple macrostates with different internal energy at the same temperature. The points of zero slope indicate locations of mechanical instability in the canonical ensemble.

A further loosening of the confinement introduces points on the caloric curve with infinite slope, indicating the presence of multiple macrostates at different temperature with the same internal energy. Such points are well known to be associated with mechanical instabilities in the microcanonical ensemble [11]. Both types of instabilities point to hysteretic behavior

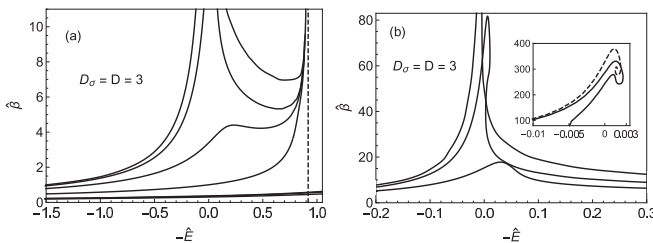


FIG. 9. Caloric curves of FD clusters with spherical symmetry with confining radius (a) $\hat{R} = 0.648, 3.01, 14.0, 64.8$, (b) $\hat{R} = 14.0, 64.8, 301$. The inset zooms into a part of the curve for $\hat{R} = 301$ (named dinosaur's neck [11]) not shown in the main plot and compares it with a similar feature of the MB caloric curve (dashed line).

of one-phase macrostates (Sec. VI), but they also point to the possibility of phase coexistence (Sec. VII), a phenomenon hitherto unexplored.

VI. EMERGENT DEGENERACY

We have seen that density profiles of fully degenerate finite-mass FD clusters have compact support. This is no longer the case for equilibrium macrostates at nonzero temperature. The cluster surfaces becomes fuzzy—an attribute related to the absence of short-range cohesive forces in our modeling. The density profile acquires a tail out to infinite distances from the center of the cluster. Wall confinement becomes necessary to equilibrate finite-mass clusters at nonzero temperature in some cases.

A. Asymptotics of self-confined clusters

It is instructive to take a look at the asymptotic decay laws of density profiles up front. The exact analysis, which follows the approach of Ref. [40], starts from

$$\frac{\hat{z}'(\hat{r})}{\hat{z}(\hat{r})} \hat{r}^{\mathcal{D}_\sigma - 1} = -\frac{2\mathcal{D}_\sigma}{\hat{T}} \int_0^{\hat{r}} d\hat{r}' \hat{r}'^{\mathcal{D}_\sigma - 1} \rho(\hat{r}'), \quad (46)$$

inferred from Eqs. (2), (3), and (4c). With Eq. (15) we can write

$$\frac{\hat{z}'(\hat{r})}{\hat{z}(\hat{r})} \hat{r}^{\mathcal{D}_\sigma - 1} = -\frac{2}{\hat{T}} \left[1 - \int_{\hat{r}}^{\infty} d\hat{r}' \hat{r}'^{\mathcal{D}_\sigma - 1} \rho(\hat{r}') \right]. \quad (47)$$

The finite-mass condition for density profiles with power-law decay is a lower bound for the exponent

$$\rho(\hat{r}) \sim \hat{r}^{-\eta}, \quad \eta > \mathcal{D}_\sigma. \quad (48)$$

This condition ensures that the integral in Eq. (47) becomes negligibly small at large \hat{r} . In the low-density asymptotic regime we have $\hat{z}'/\hat{z} = \rho'/\rho$. We thus extract from Eq. (47) the limit,

$$\lim_{\hat{r} \rightarrow \infty} \frac{\rho'(\hat{r})}{\rho(\hat{r})} \hat{r}^{\mathcal{D}_\sigma - 1} = -\frac{2}{\hat{T}}, \quad (49)$$

which only depends on the symmetry of the cluster, but not on the dimensionality of the space. The solution of Eq. (49) yields exponential asymptotics for planar clusters,

$$\rho(\hat{r})_{\text{as}} \sim e^{-2\hat{r}/\hat{T}} : \mathcal{D}_\sigma = 1, \quad (50)$$

and power-law asymptotics for cylindrical clusters,

$$\rho(\hat{r})_{\text{as}} \sim \hat{r}^{-2/\hat{T}} : \mathcal{D}_\sigma = 2. \quad (51)$$

The finite-mass condition (48) restricts the temperature range for the power-law asymptotics (51) to $0 < \hat{T} < 1$. We shall see that the self-confinement condition for cylindrical clusters is more stringent and restricts power-law asymptotics to $0 < \hat{T} < \frac{1}{2}$.

Self-confined clusters with spherical symmetry at nonzero temperature only exist if they have infinite mass. The leading asymptotic decay of the density profile is independent of temperature in this case [2]:

$$\rho(\hat{r})_{\text{as}} \sim 2\hat{r}^{-2} : \mathcal{D}_\sigma = 3. \quad (52)$$

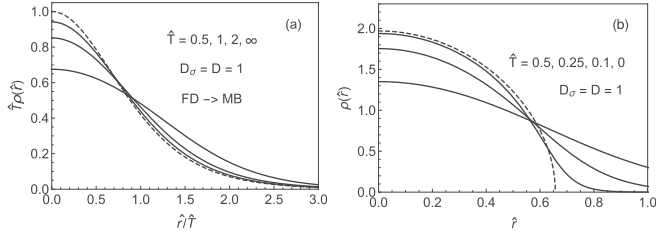


FIG. 10. (a) Rescaled density profiles of the FD gas in $\mathcal{D}_\sigma = \mathcal{D} = 1$ at high \hat{T} . The dashed line represents the MB profile (53), which is independent of \hat{T} in rescaled units. (b) Density profiles of FD clusters at low \hat{T} . The dashed line represents the $\hat{T} = 0$ profile from Sec. IV A.

B. Planar symmetry

It is well known that an unconfined MB cluster with planar symmetry remains stable against evaporation or gravitational collapse at any nonzero temperature. The exact density profile is [40–46]

$$\rho(\hat{r})_{\text{MB}} = \frac{1}{\hat{T}} \operatorname{sech}^2\left(\frac{\hat{r}}{\hat{T}}\right). \quad (53)$$

The exponential FD asymptotics (50) is also realized in the MB profile (53), as expected. With decreasing \hat{T} , $\rho(\hat{r})_{\text{MB}}$ gradually becomes narrower and more strongly peaked at the central plane of the cluster, approaching a δ -function in the limit $\hat{T} \rightarrow 0$. Deviations of the FD density profile from the MB result (53) are expected to emerge gradually. The exclusion principle kicks into action when the (local) average interparticle distance becomes comparable to the thermal wavelength. This criterion is first met near the center of the cluster, where the density is highest.

The central density of the FD cluster is indeed suppressed relative to that of an MB cluster as shown in Fig. 10(a). The dashed line represents the universal MB density profile in rescaled units. The solid lines illustrate how the FD density profile (for $\mathcal{D} = 1$) deviates from it as the temperature is being lowered from a high value. The MB result is independent of \mathcal{D} . The FD deviations are similar in $\mathcal{D} = 2, 3$ (not shown), albeit somewhat slower with increasing \mathcal{D} , as might be expected.

The \mathcal{D} -dependence of the FD profiles becomes more conspicuous at low \mathcal{D} as shown in Figs. 10(b) and 11. The solutions of the ODE (13) at $\hat{T} > 0$ converge neatly toward the solutions of the ODE (17) at $\hat{T} = 0$. The density of particles at large distances is exponentially suppressed according to

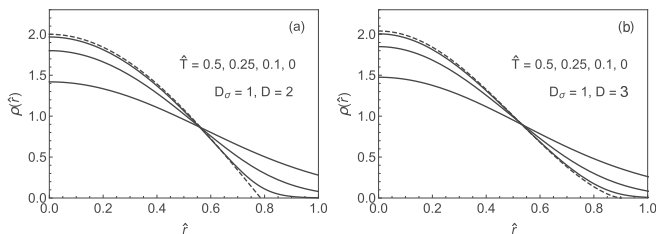


FIG. 11. Density profiles of planar FD gas in (a) $\mathcal{D} = 2$ and (b) $\mathcal{D} = 3$ at low \hat{T} . The dashed lines represent the $\hat{T} = 0$ profiles from Sec. IV B and Sec. IV C, respectively.

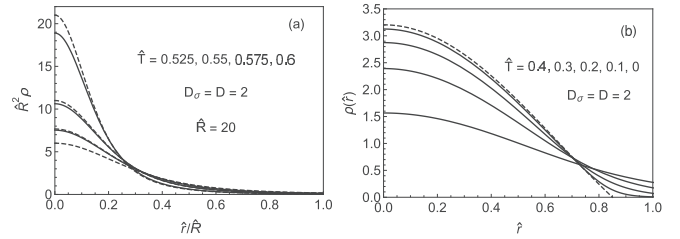


FIG. 12. (a) Rescaled FD density profiles in $\mathcal{D}_\sigma = \mathcal{D} = 2$ at $\hat{T} > \hat{T}_{\text{MB}}$ in a disk-shaped space. The dashed line represents the MB profile (55). (b) Scaled FD density profiles at $\hat{T} < \hat{T}_{\text{MB}}$ in an unconfined space. The dashed line represents the $\hat{T} = 0$ profile from Sec. IV D.

Eq. (50) in all \mathcal{D} , but the limiting $\hat{T} = 0$ profile strongly depends on \mathcal{D} .

C. Cylindrical symmetry

MB gas clusters with cylindrical symmetry, which we again use as a benchmark, are vulnerable to both particle escape and gravitational collapse. In a wall-confined space of radius \hat{R} —a disk in $\mathcal{D} = 2$ or a cylinder in $\mathcal{D} = 3$ —MB clusters are stable against gravitational collapse for temperatures above the threshold value [40,45–57],

$$\hat{T}_{\text{MB}} = \frac{1}{2}. \quad (54)$$

The exact density profile reads [40,45]:

$$\rho(\hat{r})_{\text{MB}} = \frac{1}{\hat{R}^2} \frac{2\hat{T}(2\hat{T} - 1)}{[(\hat{r}/\hat{R})^2 + 2\hat{T} - 1]^2}. \quad (55)$$

A one-parameter family of density profiles exists in the combined limit,

$$\hat{T} \rightarrow \hat{T}_{\text{MB}}, \quad \hat{R} \rightarrow \infty, \quad \frac{\hat{T}^2}{2\hat{R}^2(2\hat{T} - 1)} \rightarrow c > 0, \quad (56)$$

at the border between collapse or escape [40,46]:

$$\rho(\hat{r})_{\text{MB}} = \frac{4c}{\hat{T}_{\text{MB}}} \left[1 + 2c \left(\frac{\hat{r}}{\hat{T}_{\text{MB}}} \right)^2 \right]^{-2}. \quad (57)$$

This includes the collapsed state ($c \rightarrow \infty$) and the evaporated state ($c \rightarrow 0$). The density profile (57) of this precarious MB state without wall confinement does exhibit the power-law asymptotics (51) for the FD cluster, albeit only at the threshold temperature. FD clusters with cylindrical symmetry are equally vulnerable to particle escape, but not to gravitational collapse. Whereas the MB profile (55) acquires an unlimited central density as \hat{T} approaches \hat{T}_{MB} from above, the FD particles resist such squeezing on account of the exclusion principle.

For the sake of brevity, we focus on dimension $\mathcal{D} = 2$. The results for $\mathcal{D} = 3$ are very similar except in the limit $\hat{T} \rightarrow 0$ (Sec. IV D). Connecting the FD solutions of (13) with the MB result (55) graphically again requires some rescaling, as shown in Fig. 12(a). The choice of a large \hat{R} facilitates a convergence between FD and MB profiles not far above \hat{T}_{MB} . The approach of the FD profiles $T > 0$ toward the $\hat{T} = 0$ profile from Sec. IV D is shown in Fig. 12(b) using different scales.

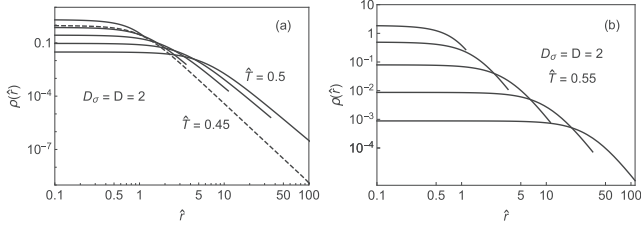


FIG. 13. Density profiles for the FD cluster with $D_\sigma = \mathcal{D} = 2$ at (a) $\hat{T} = 0.45$ (dashed line), $\hat{T} = 0.5$ (solid lines) and (b) $\hat{T} = 0.55$. The radius of wall confinement, $\hat{R} = 1.12, 3.54, 11.2, 35.4, 112$ is indicated by the endpoint of each solid curve.

The presence of self-confinement at $\hat{T} < \hat{T}_{\text{MB}}$ and its absence at $\hat{T} > \hat{T}_{\text{MB}}$ are illustrated in Fig. 13 from a different angle [40]. When we widen the space for the gas at constant sub-threshold temperature $\hat{T} = 0.45$ by isothermally increasing the radius \hat{R} , the profile shows virtually no response [dashed line in Fig. 13(a)]. At that temperature, self-confinement is robust and the observed power-law decay is in accord with the asymptotics (51).

When the wall confinement is quasistatically and isothermally relaxed at \hat{T}_{MB} , the cluster responds differently as shown by the solid lines in Fig. 13(a). A power-law tail, $\sim \hat{r}^{-4}$, survives and becomes increasingly conspicuous for large \hat{R} , in agreement with the asymptotics (51). What makes the profile at \hat{T}_{MB} qualitatively different from the sub-threshold profiles is the presence of a flat portion of increasing width and decreasing height around the center of the cluster. Self-confinement is no longer operational.

Whereas self-confinement is already absent at \hat{T}_{MB} , the structure of density profiles is yet different at higher temperatures such as shown in Fig. 13(b) for $\hat{T} = 0.55$. Here the flat portion becomes more dominant, extending over a wider region, and the power-law tail has disappeared. The only evidence of gravity is the reduced density near the wall.

There are no abrupt changes when a wall-confined FD cluster with cylindrical symmetry is heated up or cooled down quasistatically. This trait is shared with planar clusters, where wall-confinement is not even necessary. An unconfined FD cluster with cylindrical symmetry will spread out gradually when heated up. Its density will become low everywhere before \hat{T}_{MB} is reached, at which point it will behave MB-like.

Confinement with a wide radius \hat{R} makes it possible to observe a crossover between density profiles that can be interpreted as incipient escape. Within a relatively short interval of rising \hat{T} , the density profile changes from a core/halo variety to flat variety (Fig. 13). This crossover has also been seen in the caloric curves (Fig. 8). We shall see next that a switch from cylindrical to spherical symmetry impacts both the MB and the FD clusters qualitatively, but in quite different ways.

D. Spherical symmetry

Here the inequivalence of ensembles matters, as the structure of caloric curves made clear (Sec. V). For the sake of brevity, our focus will be on the canonical ensemble. Analogous reasoning produces corresponding results for the microcanonical ensemble. Spherical gas clusters of finite mass

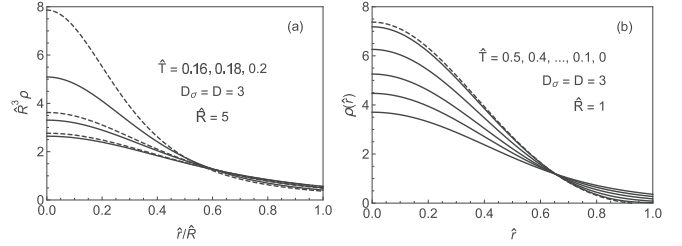


FIG. 14. (a) Density profiles of a confined FD gas (solid curves) and MB gas (dashed curves) in $D_\sigma = \mathcal{D} = 3$ at temperatures near \hat{T}_C . (b) Density profile of an FD gas on approach to the fully degenerate limiting case (dashed curve). Wall confinement turns into self-confinement at $\hat{T} = 0$.

at nonzero temperature must be stabilized against escape by wall confinement. This attribute is independent of statistics. For the stability against gravitational collapse, the statistics does matter, of course. The finite-mass MB cluster is only stable above a threshold temperature which depends on the radius of confinement [3,9,15,18],

$$\hat{T}_C = \frac{\hat{T}_C}{\hat{R}}, \quad \hat{T}_C = 0.794422 \dots \quad (58)$$

Unlike in the case of cylindrical symmetry (Sec. VIC), where, on the verge of collapse, the MB gas is highly concentrated at the center of the cluster, the density profile of a spherical MB cluster at the point of collapse is still broad with the gas pushing against the wall.

In the caloric curves of cylindrical FD clusters we have noted an incipient instability for large \hat{R} around \hat{T}_{MB} , where the MB cluster undergoes a real instability. We shall see that spherical FD clusters under tight confinement behave similarly, but now in the vicinity of \hat{T}_C , where the spherical MB cluster collapses. Under more loose confinement, by contrast, the spherical FD cluster exhibits a real instability, again near \hat{T}_C , yet very unlike the MB instability.

We begin our analysis of the spherical FD cluster with finite mass by establishing the contacts with the high- T and low- T anchor points. In Fig. 14(a) we compare density FD and MB profiles as \hat{T} approaches \hat{T}_C from above. The defenses against compression are getting weaker in the MB gas and stronger in the FD gas. At the lowest \hat{T} , the collapse of the former is imminent. In Fig. 14(b) we show the convergence of the latter to the fully degenerate profile discussed in Sec. IV F.

For the transformation of high-temperature profiles [Fig. 14(a)] into low-temperature profiles [Fig. 14(b)] and vice versa we distinguish between a regime (i) of tight confinement and a regime (ii) of loose confinement. In regime (i) for small \hat{R} , the density profile is unique at all temperatures and evolves gradually between the high- \hat{T} MB-like profile and the self-confined Fermi ball in the low- \hat{T} limit. In regime (ii) for large \hat{R} , on the other hand, there exists a temperature interval with multiple coexisting solutions of Eq. (13). No smooth and continuously varying density profile across that interval exists. Singular behavior is inevitable when the cluster is quasistatically heated up or cooled down.

We have located the border between the two regimes at $\hat{R}_C \simeq 2.655$. In the following, we compare one case from each regime. We pick $\hat{R} = 2$ for regime (i) and $\hat{R} = 4$ for regime

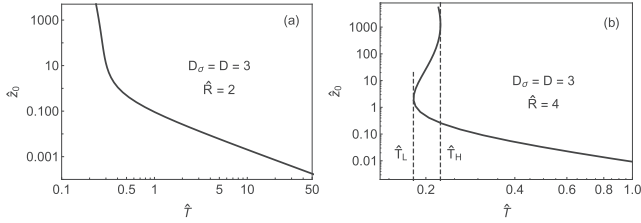


FIG. 15. Fugacity \hat{z}_0 at the center of the cluster versus scaled temperature \hat{T} for the cases with (a) $\hat{R} = 2$ and (b) $\hat{R} = 4$. The values of local extrema in (b) are $\hat{T}_L \simeq 0.182$ and $\hat{T}_H \simeq 0.224$. Both curves continue with negative slope toward $\hat{T} = 0$ and $\hat{z}_0 \rightarrow \infty$.

(ii). In case (i), \hat{z}_0 is a single-valued monotonic function of \hat{T} and in case (ii) a multiple-valued monotonic function (Fig. 15). This means that the density profile is unique at all temperatures in case (i) and at temperatures $\hat{T} < \hat{T}_L$ or $\hat{T} > \hat{T}_H$ in case (ii). However, between the temperatures \hat{T}_L and \hat{T}_H in case (ii), there exist three coexisting profiles.

In Fig. 16 we show how the density profiles evolve across a range of temperatures for cases (i) and (ii). Figure 16(a) depicts profiles across an interval of \hat{T} where the most rapid (yet still gradual) change occurs. As \hat{T} is being lowered, dominance shifts gradually from thermal fluctuations (dispersing agent) to gravity (aggregating agent). The latter is, in turn, counteracted by the exclusion principle (agent akin to steric repulsion).

In Fig. 16(b) we show three coexisting density profiles for temperatures from the interval $\hat{T}_L < \hat{T} < \hat{T}_H$. In this case, lowering \hat{T} has a more dramatic effect. At $\hat{T} > \hat{T}_H$ the only solution is a flat profile ρ_g , similar to the ones shown. The profile ρ_g represents a gaseous phase. At \hat{T}_H two additional solutions emerge. Initially the two solutions are identical, then evolve differently. The solution ρ_d represents a degenerate cluster surrounded by a gaseous halo with a fuzzy interface. The solution ρ_i (shown dashed) represents an unstable intermediate profile.

The stability status of the three solutions is most evident in Fig. 17, which shows the free energy versus temperature. Near and below \hat{T}_H , the solution ρ_g is stable and the solution ρ_d is metastable. At \hat{T}_i the stability status between the solutions switches. Here the free energies associated with the profiles ρ_g and ρ_d cross each other while the unstable profile ρ_i

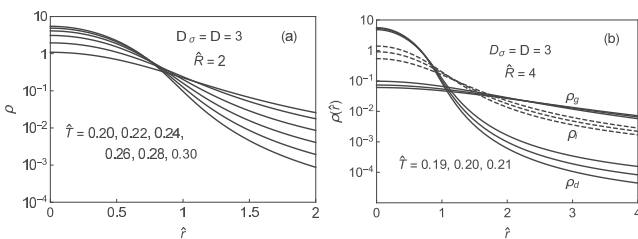


FIG. 16. Density profiles at specific scaled temperatures \hat{T} for (a) $\hat{R} = 2$ and (b) $\hat{R} = 4$. The three sets of profiles in panel (b) named ρ_g , ρ_i , and ρ_d , represent gaseous profiles, (unstable) intermediate profiles, and profiles with a degenerate core and a gaseous halo, respectively. The intercept of the solid (dashed) curves decreases (increases) with rising \hat{T} .

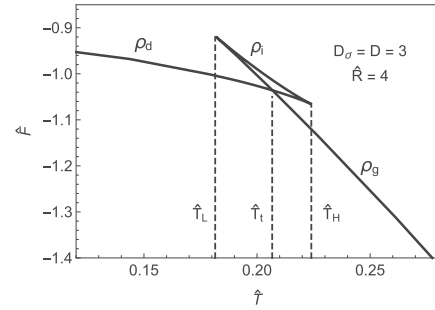


FIG. 17. Free energy versus temperature of the macrostates with central fugacities as shown in Fig. 15(b). The three branches correspond to profiles identified in Fig. 16(b). The crossing point is at $\hat{T}_i \simeq 0.207$.

a higher free energy. Below \hat{T}_i the stable profile is ρ_d . It will gradually evolve into the $T = 0$ profile analyzed earlier. The metastable solution ρ_g and the unstable solution ρ_i merge at \hat{T}_L , where both disappear.

Notice the similarity to and difference from the MB gas. Cooling precipitates an abrupt change in both cases. In the MB case that change is a gravitational collapse. In the FD case, it is a partial collapse, arrested midway by the repulsive short-range interaction, which is rooted in the exclusion principle.

It is tempting to identify the temperature \hat{T}_i as the point of a first-order transition and the temperatures \hat{T}_H , \hat{T}_L as spinodal points. The significance of \hat{T}_i is doubtful for two reasons stated below. The values \hat{T}_H , \hat{T}_L , on the other hand, correspond to points of zero slope in the caloric curve. The Poincaré turning point criterion [58] identifies them as points of mechanical instability associated with a canonical ensemble (Sec. V). Decreasing the value of \hat{R} within regime (ii) toward $\hat{R}_c \simeq 2.655$ makes the values of \hat{T}_H and \hat{T}_L move closer together and merge at the border to regime (i).

Chavanis [21] pointed out that the lifetimes of metastable states such as investigated here are extremely long. For all practical purposes, they can be treated as stable macrostates. Processes that require the transport of matter over significant energy barriers across large distances are very slow. This is the first reason that undermines the significance of \hat{T}_i . The second reason is that first-order transitions at constant \hat{T} are only generic in homogeneous systems. No quasistatic processes have yet been identified between macrostates with density profiles ρ_g and ρ_d .

VII. PHASE COEXISTENCE

The conclusions reached in the preceding paragraph do not rule out the existence of a two-phase macrostate composed of segments of different solutions of the ODE (13) with boundary conditions that satisfy the applicable stability conditions. The very long lifetimes of metastable single-phase macrostates do not speak against this possibility. An incipient cluster can evolve from very diverse initial configurations. A cluster may very well settle into a two-phase macrostate if such a state has a lower free energy at a given temperature than either of the single-phase macrostates.

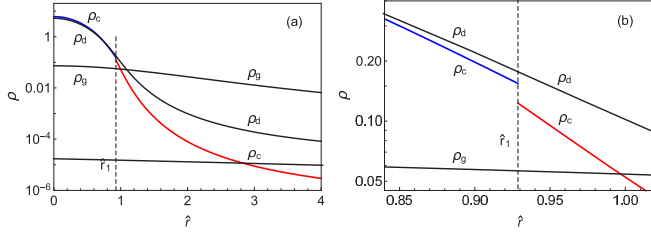


FIG. 18. Mechanically stable density profiles at temperature $\hat{T} = 0.2$ for a spherical cluster with $\hat{R} = 4$. The one-phase profiles are labeled ρ_g and ρ_d . The two-phase profile ρ_c is discontinuous at $\hat{r}_1 = 0.929$. (a) Full range of scaled distance \hat{r} . (b) Zoomed-in view of the same data.

A. Conditions for single phase boundary

A density profile (in $\mathcal{D}_\sigma = \mathcal{D} = 3$) with confinement at radius \hat{R} and one phase boundary at radius \hat{r}_1 results from a pair of solutions of the ODE (13) at given \hat{T} . Six specifications need to be fixed. The two parameters,

$$\hat{r}_1, \quad \varphi \doteq \frac{m_1}{m_{\text{tot}}}, \quad (59)$$

locate the phase boundary and determine the mass fraction of the inner phase. Additionally, there are the four boundary conditions,

$$\hat{z}(0), \quad \hat{z}'(0), \quad \hat{z}(\hat{r}_1), \quad \hat{z}'(\hat{r}_1). \quad (60)$$

The two local conditions,

$$\hat{z}'(0) = 0, \quad \hat{z}'(\hat{r}_1) = -\frac{2}{\hat{T}} \frac{\varphi}{\hat{r}_1} \hat{z}(\hat{r}_1), \quad (61)$$

satisfy smoothness at the center and guarantee mechanical stability at the phase boundary, whereas the two integral conditions,

$$\int_0^{\hat{r}_1} d\hat{r} \hat{r}^2 \rho_v(\hat{r}) = \varphi, \quad \int_{\hat{r}_1}^{\hat{R}} d\hat{r} \hat{r}^2 \rho_v(\hat{r}) = 1 - \varphi, \quad (62)$$

determine the mass fractions and guarantee that the total mass is conserved. These four conditions give us a two-parameter family of two-phase profiles separated by one phase boundary.

B. Two-phase density profile

The phase boundary is necessarily associated with a discontinuity in density—a step down over a distance short compared to the (rather long) length scale in use. Our task is to search for two-phase solutions within the temperature interval $\hat{T}_L < \hat{T} < \hat{T}_H$, where a stable and a metastable one-phase solution are known to exist.

Here we merely show evidence that two-phase solutions do indeed exist and that such solutions have a lower free energy than the single-phase solutions at the same temperature. In Fig. 18 we show the data for one representative case.

The smooth one-phase profiles are again labeled ρ_g for the gaseous type and ρ_d for the core-halo type. Their free energies are

$$\hat{F}_g = -1.003, \quad \hat{F}_d = -1.026, \quad (63)$$

respectively. The two-phase profile, labeled ρ_c , has a step-down discontinuity at $\hat{r}_1 = 0.929$. Most importantly its free energy,

$$\hat{F}_c = -1.062, \quad (64)$$

is lower than that of either single-phase profile.

Among the two-parameter family of two-phase solutions at fixed \hat{T} , one has the lowest-free-energy. We expect the two-phase solution with the lowest-free-energy to merge with a type- ρ_d one-phase solution at \hat{T}_L and to merge with a type- ρ_g one-phase solution at \hat{T}_H . These expectations, if confirmed, do not yet prove that the equilibrium state in that temperature interval has a single phase boundary. The nontrivial mechanical stability condition may very well favor a state with more than one phase boundary.

If a first-order transition between type- ρ_g and type- ρ_d single-phase profiles exists, then that transition takes place over a range of temperatures, most likely the entire interval $\hat{T}_L < \hat{T} < \hat{T}_H$. Working out such a scenario in detail is computationally demanding. It will have to include the analysis on length scales sufficiently short to resolve the structure of the phase boundary between gaseous phases. This will be the project of a separate publication.

VIII. CONCLUSION AND OUTLOOK

The shape of density profiles for self-gravitating clusters of nonrelativistic FD gases depends on both the symmetry of the cluster and the dimensionality of the space. We have analyzed six combinations of the two attributes across the full range of temperature—from fully degenerate clusters with compact support to the MB limit of low-density clusters. The length scale introduced for this study turns all density profiles at given temperature into universal curves, independent of the total mass. This length scale and the associated energy scale are equally useful for the study of BE clusters as demonstrated in a companion paper [37].

We have extended the list of analytic expressions for exact density profiles of degenerate clusters to four and identified the important specifications for all six cases, including the mass-radius relation and the cusp singularity of the density profile at the surface of the cluster. The distinct dependence of the cluster radius on the kinetic mass, the gravitational mass, and the number of particles is potentially useful in dark matter research.

Cooling down a cluster quasistatically from high temperature changes the density profile in ways that strongly depend on the symmetry and weakly on the dimensionality. For clusters with planar symmetry, the evolution of the density profile from the MB profile with exponential tails into a fully degenerate compact Fermi slab is very gradual and without landmarks. No wall confinement is necessary at any temperature.

Clusters with cylindrical symmetry, by contrast, require wall confinement against escape above a certain threshold temperature. Below that threshold, the density profiles have power-law tails with temperature-dependent exponents. Cooling down a wall-confined cylindrical cluster across the threshold temperature produces an accelerated change in the density profile—an incipient gravitational collapse,

softly arrested midway by the implications of FD statistics. An attribute shared by cylindrical and planar clusters is that mechanically stable macrostates are unique at any temperature.

Finite clusters with spherical symmetry, which need wall confinement at all nonzero temperatures, do not, in general, share this last attribute. We have identified regimes with two mechanically stable macrostates—one thermally stable and the other metastable—across a finite interval of temperature. Cooling down and heating up a cluster across this interval causes mechanical instabilities at its far end, thus producing effects of hysteresis. We have identified, inside this temperature interval, the existence of a two-phase macrostate with one phase boundary, which has a lower-free-energy than either one-phase macrostate. We have sketched a scenario of a first-order transition starting at one end of the temperature interval and reaching completion at the other end.

Investigating self-gravitating FD and BE clusters on a common length scale facilitates comparative studies such as intended here and in Ref. [37]. FD clusters and BE clusters have a common MB limit at high temperature, but evolve differently upon cooling. BE clusters lack the robustness of

FD clusters against gravitational pressure. Condensation is initiated at a nonzero temperature in all cases. The critical singularities depend on the symmetry of the cluster and dimensionality of the space [37].

A natural extension of this work will investigate a succession of relativistic effects, first the consequences of a relativistic energy-momentum relation and then the consequences of general relativity. In the first part, currently in the works [38], we demonstrate the crossover of $T = 0$ density profiles between universal nonrelativistic shapes and universal ultrarelativistic shapes. We also investigate how the mass-radius relation varies with the symmetry of the cluster and the dimensionality of the space and how the stability of spherical FD clusters depend on mass and temperature.

APPENDIX A: ALTERNATIVE SCALING CONVENTION

Here we establish, for the sake of transparency, the relations between the length scale and energy scale used in Ref. [24] and the scaling conventions introduced in Sec. III for this work. We begin by stating the explicit dependence of the length scale r_s and the energy scale $k_B T_s$ used in this work as inferred from Eqs. (12):

$$(k_B T_s)^{1+\mathcal{D}/\mathcal{D}_\sigma-\mathcal{D}/2} = \frac{1}{2} G_{\mathcal{D}} \frac{\mathcal{A}_{\mathcal{D}}}{\mathcal{D}_\sigma} \left(\frac{\mathcal{A}_{\mathcal{D}_\sigma}}{\mathcal{D}_\sigma} \right)^{-2/\mathcal{D}_\sigma} (2\pi \hbar^2)^{\mathcal{D}/\mathcal{D}_\sigma-\mathcal{D}/2} M^2 m^{-\mathcal{D}/\mathcal{D}_\sigma+\mathcal{D}/2} \tilde{N}^{2/\mathcal{D}_\sigma}, \quad (\text{A1})$$

$$r_s^{\mathcal{D}_\sigma} = \frac{\mathcal{D}_\sigma}{\mathcal{A}_{\mathcal{D}_\sigma}} (2\pi \hbar^2)^{\mathcal{D}/2} \tilde{N} m^{-\mathcal{D}/2} (k_B T_s)^{-\mathcal{D}/2}. \quad (\text{A2})$$

The alternative scaled length (for $\mathcal{D}_\sigma = \mathcal{D}$) is defined as follows (in our units):

$$\xi \doteq \frac{r}{r_P}, \quad r_P^2 = \frac{k_B T \lambda_T^{\mathcal{D}}}{g_s \mathcal{A}_{\mathcal{D}} G_{\mathcal{D}} m^2} \Gamma(\mathcal{D}/2). \quad (\text{A3})$$

In the limit $T \rightarrow 0$, the length scale r_P shrinks to zero in $\mathcal{D} = 1$, stretches to infinity in $\mathcal{D} = 3$, and is T -independent in $\mathcal{D} = 2$. Its relation to r_s from Eq. (12) is

$$\left(\frac{r_P}{r_s} \right)^2 = \frac{\Gamma(\mathcal{D}/2)}{2\mathcal{D}g_s} \hat{\Gamma}^{1-\mathcal{D}/2}. \quad (\text{A4})$$

The bridge between our ODE (7) for the fugacity $z(r)$ and the corresponding ODE arrived at in Ref. [24] is spanned as follows. We write

$$z_\xi(\xi) \doteq z(r), \quad z'_\xi = z' r_P, \quad z''_\xi = z'' r_P^2, \quad (\text{A5})$$

which transcribes Eq. (7) into

$$\frac{z''_\xi}{z_\xi} + \frac{\mathcal{D}-1}{\xi} \frac{z'_\xi}{z_\xi} - \left(\frac{z'_\xi}{z_\xi} \right)^2 + \Gamma(\mathcal{D}/2) f_{\mathcal{D}/2}(z_\xi) = 0. \quad (\text{A6})$$

With the relation,

$$z_\xi^{-1}(\xi) = k e^{\psi(\xi)}, \quad (\text{A7})$$

between the fugacity and the potential $\psi(\xi)$ the ODE (A6) becomes

$$\frac{1}{\xi^{\mathcal{D}-1}} \frac{d}{d\xi} \left(\xi^{\mathcal{D}-1} \frac{d\psi}{d\xi} \right) = I_{\mathcal{D}/2-1}(k e^{\psi(\xi)}), \quad (\text{A8})$$

where $I_n(t) = \Gamma(n-1) f_{n+1}(t^{-1})$. Both scaling conventions produce one-parameter families of solutions. The parameter only enters one of the boundary conditions. For Eq. (A8) that parameter is k and for (A6) it is $z_\xi(0)$.

Either parameter, k or $z_\xi(0)$, contains several physical quantities that we might wish to vary separately: the confining radius R , the temperature T , and the number N of particles (or the total mass $m_{\text{tot}} = NM$). In Refs. [24] the parameter k is split into two (dimensionless) parts. One is the scaled radius of confinement,

$$\alpha \doteq \frac{R}{r_P}, \quad (\text{A9})$$

and the other the degeneracy parameter,

$$\mu \doteq \eta_0 \mathcal{A}_{\mathcal{D}}^2 2^{\mathcal{D}/2-1} G_{\mathcal{D}}^{\mathcal{D}/2} m_{\text{tot}}^{\mathcal{D}/2-1} R^{\mathcal{D}(4-\mathcal{D})/2}. \quad (\text{A10})$$

The energy scale used in Refs. [24] can be stated as follows:

$$\eta^{-1} \doteq \frac{k_B T}{k_B T_P}, \quad k_B T_P = \frac{G_{\mathcal{D}} m m_{\text{tot}}}{R^{\mathcal{D}-2}}. \quad (\text{A11})$$

Its relation to $k_B T_s$ from Eqs. (12) and (A11) is

$$\frac{T_P}{T_s} = 2 \hat{R}^{2-\mathcal{D}}. \quad (\text{A12})$$

The scaled temperatures are related via

$$\eta^{-1} = \frac{1}{2} \hat{R}^{\mathcal{D}-2} \hat{T}. \quad (\text{A13})$$

The scaled radius of confinement α is T -dependent whereas \hat{R} is not. The two are related as follows:

$$\alpha = \sqrt{\frac{2\mathcal{D}g_s}{\Gamma(\mathcal{D}/2)}} \hat{T}^{(\mathcal{D}/2-1)/2} \hat{R}. \quad (\text{A14})$$

It is useful to express the degeneracy parameter μ in terms of the scaled radius of confinement α and the scaled inverse temperature η :

$$\mu = \alpha^2 \eta^{\mathcal{D}/2-1}. \quad (\text{A15})$$

The relation between μ and \hat{R} then follows directly:

$$\mu = 2^{\mathcal{D}/2} \frac{\mathcal{D}g_s}{\Gamma(\mathcal{D}/2)} \hat{R}^{2\mathcal{D}-\mathcal{D}^2/2}. \quad (\text{A16})$$

Caloric curves can be produced alternatively by keeping μ fixed and varying α (as done in Ref. [24]) or by keeping \hat{R} fixed and varying \hat{T} (as done in Sec. V). The two sets are not identical, but there is a one-on-one correspondence between maxima, minima, and locations of infinite slope. Note that the scale T_s depends on \hbar but not on R ; it is adapted to the large domain limit $R \rightarrow \infty$. By contrast, the scale T_p depend on R but not on \hbar ; it is adapted to the classical limit $\hbar \rightarrow 0$.

APPENDIX B: VIRIAL THEOREM

Here we develop an expression for the virial theorem pertaining to clusters with $\mathcal{D}_\sigma < \mathcal{D}$ in generalization to the results for $\mathcal{D}_\sigma = \mathcal{D}$ previously established by Chavanis and Sire [39]. We begin with the definition of the virial for the gravitational force,

$$\mathcal{V}_{\mathcal{D}_\sigma, \mathcal{D}} \doteq m \int d^{\mathcal{D}}r \rho_v \mathbf{r} \cdot \nabla \Phi. \quad (\text{B1})$$

The gravitational potential Φ is inferred from Eq. (3) via

$$\frac{d}{dr} \Phi(r) = -g(r) = \frac{\mathcal{A}_{\mathcal{D}}}{\mathcal{A}_{\mathcal{D}_\sigma}} \frac{G_{\mathcal{D}} \tilde{M}(r)}{r^{\mathcal{D}_\sigma-1}}, \quad (\text{B2})$$

where

$$\tilde{M}(r) \doteq \frac{M(r)}{L^{\mathcal{D}-\mathcal{D}_\sigma}} = m \mathcal{A}_{\mathcal{D}_\sigma} \int_0^r dr' r'^{\mathcal{D}_\sigma-1} \rho_v(r'). \quad (\text{B3})$$

We can thus simplify the integral in Eq. (B1):

$$\mathcal{V}_{\mathcal{D}_\sigma, \mathcal{D}} = \frac{\mathcal{A}_{\mathcal{D}}}{\mathcal{A}_{\mathcal{D}_\sigma}} \frac{G_{\mathcal{D}} L^{\mathcal{D}-\mathcal{D}_\sigma}}{2} \int_0^R \frac{dr}{r^{\mathcal{D}_\sigma-2}} \frac{d}{dr} [\tilde{M}(r)]^2. \quad (\text{B4})$$

For cases with $\mathcal{D}_\sigma = 2$ the integral is simple and, alas, useless for our purpose:

$$\mathcal{V}_{2, \mathcal{D}} = \frac{\mathcal{A}_{\mathcal{D}}}{4\pi} G_{\mathcal{D}} \tilde{m}_{\text{tot}} m_{\text{tot}}, \quad (\text{B5})$$

where $\tilde{m}_{\text{tot}} \doteq m_{\text{tot}}/L^{\mathcal{D}-\mathcal{D}_\sigma}$. For cases with $\mathcal{D}_\sigma \neq 2$, an integration by parts brings the virial into the form,

$$\mathcal{V}_{\mathcal{D}_\sigma, \mathcal{D}} = \frac{\mathcal{A}_{\mathcal{D}}}{\mathcal{A}_{\mathcal{D}_\sigma}} \frac{G_{\mathcal{D}}}{2} L^{\mathcal{D}-\mathcal{D}_\sigma} \times \left[\frac{\tilde{m}_{\text{tot}}^2}{R^{\mathcal{D}_\sigma-2}} + (\mathcal{D}_\sigma - 2) \int_0^R dr \frac{[\tilde{M}(r)]^2}{r^{\mathcal{D}_\sigma-1}} \right]. \quad (\text{B6})$$

With Eq. (B2) we can relate the virial more directly to the gravitational potential:

$$\mathcal{V}_{\mathcal{D}_\sigma, \mathcal{D}} = \frac{\mathcal{A}_{\mathcal{D}} G_{\mathcal{D}} L^{\mathcal{D}-\mathcal{D}_\sigma} \tilde{m}_{\text{tot}}^2}{2 \mathcal{A}_{\mathcal{D}_\sigma} R^{\mathcal{D}_\sigma-2}} + (\mathcal{D}_\sigma - 2) \frac{\mathcal{A}_{\mathcal{D}_\sigma} L^{\mathcal{D}-\mathcal{D}_\sigma}}{2 \mathcal{A}_{\mathcal{D}} G_{\mathcal{D}}} \int_0^R dr r^{\mathcal{D}_\sigma-1} \left[\frac{d\Phi}{dr} \right]^2. \quad (\text{B7})$$

The next thread relates the gravitational potential energy W to the same $\Phi(r)$:

$$\begin{aligned} W &= \frac{m}{2} \int d^{\mathcal{D}}r \rho_v \Phi = \frac{1}{2 \mathcal{A}_{\mathcal{D}} G_{\mathcal{D}}} \int d^{\mathcal{D}}r \Phi \nabla^2 \Phi \\ &= \frac{\mathcal{A}_{\mathcal{D}_\sigma} L^{\mathcal{D}-\mathcal{D}_\sigma}}{2 \mathcal{A}_{\mathcal{D}} G_{\mathcal{D}}} \left[R^{\mathcal{D}_\sigma-1} \Phi(R) \frac{d}{dr} \Phi(R) \right. \\ &\quad \left. - \int_0^R dr r^{\mathcal{D}_\sigma-1} \left[\frac{d\Phi}{dr} \right]^2 \right], \end{aligned} \quad (\text{B8})$$

where we used the Newton-Poisson equation, $\nabla^2 \Phi = \mathcal{A}_{\mathcal{D}} G_{\mathcal{D}} m \rho_v$, in the first step, and integrated by parts in the second. We can simplify the first term in the last expression by using Eq. (B2), evaluated at R with $\tilde{M}(R) = \tilde{m}_{\text{tot}}$.

Convenient choices for the integration constants set $\Phi(0) = 0$ in $\mathcal{D}_\sigma = 1$, $\Phi(R) = 0$ in $\mathcal{D}_\sigma = 2$, and $\Phi(\infty) = 0$ in $\mathcal{D}_\sigma > 2$. The expressions, valid for $r \leq R$, read

$$\Phi(r) = -\frac{1}{(\mathcal{D}_\sigma - 2)} \frac{\mathcal{A}_{\mathcal{D}} G_{\mathcal{D}} \tilde{m}_{\text{tot}}}{\mathcal{A}_{\mathcal{D}_\sigma} r^{\mathcal{D}_\sigma-2}}, \quad : \mathcal{D}_\sigma \neq 2, \quad (\text{B9a})$$

$$\Phi(r) = \frac{\mathcal{A}_{\mathcal{D}} G_{\mathcal{D}} \tilde{M}}{2\pi} \ln\left(\frac{r}{R}\right) \quad : \mathcal{D}_\sigma = 2. \quad (\text{B9b})$$

With these substitutions, Eq. (B8) becomes

$$\begin{aligned} W &= -\frac{\mathcal{A}_{\mathcal{D}} L^{\mathcal{D}-\mathcal{D}_\sigma}}{2 \mathcal{A}_{\mathcal{D}_\sigma} (\mathcal{D}_\sigma - 2)} \frac{G_{\mathcal{D}} \tilde{m}_{\text{tot}}^2}{R^{\mathcal{D}_\sigma-2}} \\ &\quad - \frac{\mathcal{A}_{\mathcal{D}_\sigma} L^{\mathcal{D}-\mathcal{D}_\sigma}}{2 \mathcal{A}_{\mathcal{D}} G_{\mathcal{D}}} \int_0^R dr r^{\mathcal{D}_\sigma-1} \left[\frac{d\Phi}{dr} \right]^2 \quad : \mathcal{D}_\sigma \neq 2, \end{aligned} \quad (\text{B10a})$$

$$W = -\frac{\pi L^{\mathcal{D}-2}}{\mathcal{A}_{\mathcal{D}} G_{\mathcal{D}}} \int_0^R dr r \left[\frac{d\Phi}{dr} \right]^2 \quad : \mathcal{D}_\sigma = 2. \quad (\text{B10b})$$

Comparison of Eq. (B10) with Eq. (B7) yields the important intermediate result,

$$\mathcal{V}_{\mathcal{D}_\sigma, \mathcal{D}} = -(\mathcal{D}_\sigma - 2)W. \quad (\text{B11})$$

Next we establish the relationship between the virial $\mathcal{V}_{\mathcal{D}_\sigma, \mathcal{D}}$ and the kinetic energy U . We start from the condition (2) of mechanical equilibrium,

$$\nabla p = -m \rho_v \nabla \Phi, \quad (\text{B12})$$

which permits the virial (B1) to be rendered in the form,

$$\mathcal{V}_{\mathcal{D}_\sigma, \mathcal{D}} = \int d^{\mathcal{D}}r \mathbf{r} \cdot \nabla p, \quad (\text{B13})$$

and, after an integration by parts, in the form,

$$\begin{aligned} \mathcal{V}_{\mathcal{D}_\sigma, \mathcal{D}} &= -\mathcal{A}_{\mathcal{D}_\sigma} L^{\mathcal{D}-\mathcal{D}_\sigma} R^{\mathcal{D}_\sigma} p(R) \\ &+ \mathcal{D}_\sigma \mathcal{A}_{\mathcal{D}_\sigma} L^{\mathcal{D}-\mathcal{D}_\sigma} \int_0^R dr r^{\mathcal{D}_\sigma-1} p(r). \end{aligned} \quad (\text{B14})$$

The second term in this expression is related to the kinetic energy via the EOS (4), which thus produces the second intermediate result (still for $\mathcal{D}_\sigma \neq 2$),

$$2 \frac{\mathcal{D}_\sigma}{\mathcal{D}} U - \mathcal{V}_{\mathcal{D}_\sigma, \mathcal{D}} = \mathcal{A}_{\mathcal{D}_\sigma} L^{\mathcal{D}-\mathcal{D}_\sigma} R^{\mathcal{D}_\sigma} p(R). \quad (\text{B15})$$

The combination of Eqs. (B11) and (B15), which relates the potential energy and the kinetic energy for self-gravitating FD clusters with planar symmetry ($\mathcal{D} = 1$) or spherical symmetry ($\mathcal{D} = 3$), thus constitutes the virial theorem in the general form required for this study:

$$2 \frac{\mathcal{D}_\sigma}{\mathcal{D}} U + (\mathcal{D}_\sigma - 2)W = \mathcal{A}_{\mathcal{D}_\sigma} L^{\mathcal{D}-\mathcal{D}_\sigma} R^{\mathcal{D}_\sigma} p(R). \quad (\text{B16})$$

For clusters with cylindrical symmetry ($\mathcal{D}_\sigma = 2$), the combination of Eqs. (B5) and (B15) produce the identity,

$$\frac{4}{\mathcal{D}} U - \frac{\mathcal{A}_{\mathcal{D}}}{4\pi} G_{\mathcal{D}} \tilde{m}_{\text{tot}} m_{\text{tot}} = 2\pi L^{\mathcal{D}-2} R^2 p(R). \quad (\text{B17})$$

From the virial theorem, we can obtain explicit exact results in special cases:

(i) If we consider $\mathcal{D}_\sigma = 1$, $p(R) = 0$ (valid in an infinite domain or when the density profile is a Dirac distribution), and the MB statistics, from the relations $E = U + W$, $2 \frac{1}{\mathcal{D}} U - W = 0$ and $U = \frac{\mathcal{D}}{2} N k_B T$, we find that the caloric curve is given by

$$E = \left(\frac{\mathcal{D}}{2} + 1 \right) N k_B T. \quad (\text{B18})$$

(ii) If we consider $\mathcal{D}_\sigma = 2$, $p(R) = 0$ (valid in an infinite domain or when the density profile is a Dirac distribution), and the MB statistics, from the relations $\frac{4}{\mathcal{D}} U - \frac{\mathcal{A}_{\mathcal{D}}}{4\pi} G_{\mathcal{D}} \tilde{m}_{\text{tot}} m_{\text{tot}} = 0$ and $U = \frac{\mathcal{D}}{2} N k_B T$, then we find that the temperature is given by

$$k_B T = \frac{\mathcal{A}_{\mathcal{D}}}{8\pi N} G_{\mathcal{D}} \tilde{m}_{\text{tot}} m_{\text{tot}}. \quad (\text{B19})$$

APPENDIX C: POLYTROPES

Gaseous polytropes with index n are characterized by a pure power-law dependence of pressure on density:

$$p \propto \rho^\gamma, \quad \gamma = 1 + \frac{1}{n}. \quad (\text{C1})$$

Internal energy expressions for polytropes with index $n = \mathcal{D}/2$ are a useful way to characterize FD clusters in \mathcal{D} dimensions at $T = 0$. Following the strategy of Ref. [39], but including clusters with $\mathcal{D}_\sigma < \mathcal{D}$, we begin by extracting from the asymptotics carried out in Sec. IV the relation between pressure and density,

$$p(r) = \left(\frac{\Lambda^{\mathcal{D}/2} \Gamma(\mathcal{D}/2 + 1)}{g_s} \right)^{2/\mathcal{D}} \frac{\rho_v(r)^{1+2/\mathcal{D}}}{(\mathcal{D}/2 + 1)}, \quad (\text{C2})$$

which has the form (C1) and can be rendered as follows:

$$\frac{1}{\rho_v(r)} \frac{d}{dr} p(r) = (\mathcal{D}/2 + 1) \frac{d}{dr} \left(\frac{p(r)}{\rho_v(r)} \right). \quad (\text{C3})$$

Combining it with the condition (B12) of mechanical equilibrium, we obtain

$$-\frac{(\mathcal{D}/2 + 1)}{m} \frac{d}{dr} \left(\frac{p(r)}{\rho_v(r)} \right) = \frac{d}{dr} \Phi(r). \quad (\text{C4})$$

The profile of the gravitational potential thus becomes,

$$\Phi(r) = \Phi(R) - \frac{(\mathcal{D}/2 + 1)}{m} \left(\frac{p(r)}{\rho_v(r)} - \frac{p(R)}{\rho_v(R)} \right). \quad (\text{C5})$$

Expressing the internal energy $E = U + W$ and the number of particles N via the integrals,

$$E = \frac{\mathcal{D}}{2} \int d^{\mathcal{D}} r p + \frac{m}{2} \int d^{\mathcal{D}} r \rho_v \Phi, \quad N = \int d^{\mathcal{D}} r \rho_v, \quad (\text{C6})$$

we can cast the potential energy into the form,

$$W = -\frac{(\mathcal{D}/2 + 1)}{\mathcal{D}} U + \frac{(\mathcal{D}/2 + 1)N}{2} \frac{p(R)}{\rho_v(R)} + \frac{Nm}{2} \Phi(R). \quad (\text{C7})$$

Next we eliminate the kinetic energy U from Eq. (C7) by invoking the virial theorem, i.e., relations (B16) for $\mathcal{D}_\sigma \neq 2$ and (B17) for $\mathcal{D}_\sigma = 2$. We thus obtain,

$$\begin{aligned} W &= \frac{2\mathcal{D}_\sigma}{2\mathcal{D}_\sigma - (\mathcal{D}/2 + 1)(\mathcal{D}_\sigma - 2)} \\ &\times \left[-\frac{\mathcal{A}_{\mathcal{D}} G_{\mathcal{D}} \tilde{m}_{\text{tot}} m_{\text{tot}}}{2\mathcal{A}_{\mathcal{D}_\sigma} (\mathcal{D}_\sigma - 2)} R^{2-\mathcal{D}_\sigma} + \frac{N(\mathcal{D}/2 + 1)}{2} \frac{p(R)}{\rho_v(R)} \right. \\ &\left. - \frac{(\mathcal{D}/2 + 1)}{2\mathcal{D}_\sigma} \mathcal{A}_{\mathcal{D}_\sigma} L^{\mathcal{D}-\mathcal{D}_\sigma} R^{\mathcal{D}_\sigma} p(R) \right], \end{aligned} \quad (\text{C8a})$$

$$\begin{aligned} W &= \frac{N(\mathcal{D}/2 + 1)}{2} \frac{p(R)}{\rho_v(R)} - \frac{(\mathcal{D}/2 + 1)}{4} \left[\frac{\mathcal{A}_{\mathcal{D}}}{4\pi} G_{\mathcal{D}} \tilde{m}_{\text{tot}} m_{\text{tot}} \right. \\ &\left. + 2\pi L^{\mathcal{D}-2} R^2 p(R) \right], \end{aligned} \quad (\text{C8b})$$

for $\mathcal{D}_\sigma \neq 2$ and $\mathcal{D}_\sigma = 2$, respectively. We have used $\Phi(R) = -\mathcal{A}_{\mathcal{D}} G_{\mathcal{D}} \tilde{M} / [\mathcal{A}_{\mathcal{D}_\sigma} (\mathcal{D}_\sigma - 2) R^{\mathcal{D}_\sigma-2}]$ for $\mathcal{D}_\sigma \neq 2$ and $\Phi(R) = 0$ when $\mathcal{D}_\sigma = 2$. Using Eqs. (B16), (B17), and (C8) we thus simplify the internal energy expressions for $\mathcal{D}_\sigma \neq 2$ and $\mathcal{D}_\sigma = 2$ into

$$\begin{aligned} E &= \frac{\mathcal{D}}{2\mathcal{D}_\sigma} \mathcal{A}_{\mathcal{D}_\sigma} L^{\mathcal{D}-\mathcal{D}_\sigma} R^{\mathcal{D}_\sigma} p(R) + \left(1 - \frac{\mathcal{D}(\mathcal{D}_\sigma - 2)}{2\mathcal{D}_\sigma} \right) W, \\ E &= \frac{(\mathcal{D}/2 - 1)}{4} \left[\frac{\mathcal{A}_{\mathcal{D}}}{4\pi} G_{\mathcal{D}} \tilde{m}_{\text{tot}} m_{\text{tot}} + 2\pi L^{\mathcal{D}-2} R^2 p(R) \right] \\ &+ \frac{N(\mathcal{D}/2 + 1)}{2} \frac{p(R)}{\rho_v(R)}, \end{aligned} \quad (\text{C9})$$

respectively. The above expression for $\mathcal{D}_\sigma = 2$ is only useful for incomplete polytropes, where $p(R)/\rho_v(R) \neq 0$, or complete polytropes with $\mathcal{D} \neq 2$. For complete polytropes, including those where $\mathcal{D}_\sigma = \mathcal{D} = 2$, we derive an alternate expression for the potential energy. Replacing R by

r_0 , the radius marking the surface of the cluster, and using $p(r_0)/\rho_v(r_0) = 0$, Eq. (C8) reduces to the Betti-Ritter formula [2]:

$$W = \frac{-\mathcal{D}_\sigma}{2\mathcal{D}_\sigma - (\mathcal{D}/2 + 1)(\mathcal{D}_\sigma - 2)} \frac{\mathcal{A}_\mathcal{D} G_\mathcal{D} \tilde{M} M}{\mathcal{A}_{\mathcal{D}_\sigma} (\mathcal{D}_\sigma - 2)} r_0^{2-\mathcal{D}_\sigma},$$

$$W = \frac{\mathcal{A}_\mathcal{D} G_\mathcal{D} \tilde{m}_{\text{tot}} m_{\text{tot}}}{4\pi} \ln\left(\frac{r_0}{R}\right) - (\mathcal{D}/2 + 1) \frac{\mathcal{A}_\mathcal{D} G_\mathcal{D} \tilde{M} M}{16\pi}, \quad (\text{C10})$$

for $\mathcal{D}_\sigma \neq 2$ and $\mathcal{D}_\sigma = 2$, respectively. The energy for the complete polytrope can now be written in the form

$$E = -\frac{1}{2} \frac{2\mathcal{D}_\sigma - \mathcal{D}(\mathcal{D}_\sigma - 2)}{2\mathcal{D}_\sigma - (\mathcal{D}/2 + 1)(\mathcal{D}_\sigma - 2)} \frac{\mathcal{A}_\mathcal{D} G_\mathcal{D} \tilde{m}_{\text{tot}} m_{\text{tot}}}{\mathcal{A}_{\mathcal{D}_\sigma} (\mathcal{D}_\sigma - 2) r_0^{\mathcal{D}_\sigma - 2}},$$

$$E = \frac{\mathcal{A}_\mathcal{D} G_\mathcal{D} \tilde{m}_{\text{tot}} m_{\text{tot}}}{4\pi} \ln\left(\frac{r_0}{R}\right) + (\mathcal{D}/2 - 1) \frac{\mathcal{A}_\mathcal{D} G_\mathcal{D} \tilde{m}_{\text{tot}} m_{\text{tot}}}{16\pi}, \quad (\text{C11})$$

where we have used $E = U + W$ and eliminated the kinetic energy by means of the virial theorem.

- [1] R. H. Fowler, On dense matter, *Mon. Not. R. Astron. Soc.* **87**, 114 (1926).
- [2] S. Chandrasekhar, *An Introduction to the Theory of Stellar Structure* (University of Chicago Press, Chicago, IL, 1939).
- [3] R. Emden, *Gaskugeln* (Teubner Verlag, Leipzig, 1907).
- [4] E. C. Stoner, The limiting density in white dwarf stars, *London, Edinburgh Dublin Philos. Mag. J. Sci.* **7**, 63 (1929).
- [5] E. A. Milne, The analysis of stellar structure, *Mon. Not. R. Astron. Soc.* **91**, 4 (1930).
- [6] S. Chandrasekhar, The density of white dwarf stars *London, Edinburgh Dublin Philos. Mag. J. Sci.* **11**, 592 (1931).
- [7] P. Hertel and W. Thirring, Free energy of gravitating fermions, *Commun. Math. Phys.* **24**, 22 (1971).
- [8] P. Hertel and W. Thirring, Thermodynamic instability of a system of gravitating fermions. In *Quanten und Felder*, edited by H. P. Dürr (Braunschweig, Vieweg, 1971).
- [9] H. J. de Vega and N. Sanchez, Statistical mechanics of the self-gravitating gas: I. Thermodynamic limit and phase diagrams, *Nucl. Phys. B* **625**, 409 (2002).
- [10] H. J. de Vega and N. Sanchez, Statistical mechanics of the self-gravitating gas: II. Local physical magnitudes and fractal structures, *Nucl. Phys. B* **625**, 460 (2002).
- [11] P. H. Chavanis, Phase transitions in self-gravitating systems, *Int. J. Mod. Phys. B* **20**, 3113 (2006).
- [12] G. Alberti and P. H. Chavanis, Caloric curves of self-gravitating fermions in general relativity, *Eur. Phys. J. B* **93**, 208 (2020).
- [13] P. H. Chavanis, Mass-radius relation of Newtonian self-gravitating Bose-Einstein condensates with short-range interactions. I. Analytical results, *Phys. Rev. D* **84**, 043531 (2011).
- [14] V. A. Antonov, *Vest. Leningr. Gos. Univ.* **7**, 135 (1962); V. A. Antonov, Translation in *IAU Symposium* **113**, 525 (1985).
- [15] D. Lynden-Bell and R. Wood, The gravo-thermal catastrophe in isothermal spheres and the onset of red-giant structure for stellar systems, *Mon. Not. R. Astron. Soc.* **138**, 495 (1968).
- [16] J. Katz, On the number of unstable modes of an equilibrium, *Mon. Not. R. Astron. Soc.* **183**, 765 (1978).
- [17] T. Padmanabhan, Antonov Instability and Gravothermal Catastrophe—Revisited, *Astrophys. J., Suppl. Ser.* **71**, 651 (1989).
- [18] P. H. Chavanis, Gravitational instability of finite isothermal spheres, *Astron. Astrophys.* **381**, 340 (2002).
- [19] N. Bilic and R. D. Viollier, Gravitational phase transition of fermionic matter, *Phys. Lett. B* **408**, 75 (1997).
- [20] P. H. Chavanis, Phase transitions in self-gravitating systems: Self-gravitating fermions and hard spheres models, *Phys. Rev. E* **65**, 056123 (2002).
- [21] P. H. Chavanis, On the lifetime of metastable states in self-gravitating systems, *Astron. Astrophys.* **432**, 117 (2005).
- [22] P. H. Chavanis, M. Lemou, and F. Méhats, Models of dark matter halos based on statistical mechanics: The fermionic King model, *Phys. Rev. D* **92**, 123527 (2015).
- [23] P. H. Chavanis, White dwarf stars in \mathcal{D} dimensions, *Phys. Rev. D* **76**, 023004 (2007).
- [24] P. H. Chavanis, Statistical mechanics and thermodynamic limit of self-gravitating fermions in D dimensions, *Phys. Rev. E* **69**, 066126 (2004).
- [25] P. Ehrenfest, In what way does it become manifest in the fundamental laws of physics that space has three dimensions? *Proc. Amst. Acad.* **20**, 200 (1917).
- [26] S. L. Shapiro and S. A. Teukolsky, *Black Holes, White Dwarfs, and Neutron Stars* (Wiley Interscience, New York, NY, 1983).
- [27] P. H. Chavanis, Predictive model of fermionic dark matter halos with a quantum core and an isothermal atmosphere, [arXiv:2112.07726](https://arxiv.org/abs/2112.07726) [*Phys. Rev. D* (to be published)].
- [28] D. Lynden-Bell, Statistical mechanics of violent relaxation in stellar systems, *Mon. Not. R. Astron. Soc.* **136**, 101 (1967).
- [29] P. H. Chavanis, On the coarse-grained evolution of collisionless stellar systems, *Mon. Not. R. Astron. Soc.* **300**, 981 (1998).
- [30] P. H. Chavanis and J. Sommeria, Degenerate equilibrium states of collisionless stellar systems, *Mon. Not. R. Astron. Soc.* **296**, 569 (1998).
- [31] N. Bilic, F. Munyaneza, G. B. Tupper, and R. D. Viollier, The dynamics of stars near Sgr A* and dark matter at the center and in the halo of the Galaxy, *Prog. Part. Nucl. Phys.* **48**, 291 (2002).
- [32] N. Bilic, G. B. Tupper, and R. D. Viollier, Dark matter in the galaxy, *Lect. Notes Phys.* **616**, 24 (2003).
- [33] R. Ruffini, C. R. Argüelles, and J. A. Rueda, On the core-halo distribution of dark matter in galaxies, *Mon. Not. R. Astron. Soc.* **451**, 622 (2015).
- [34] C. R. Argüelles, M. I. Díaz, A. Krut, and R. Yunis, On the formation and stability of fermionic dark matter haloes in a cosmological framework, *Mon. Not. R. Astron. Soc.* **502**, 4227 (2021).
- [35] P. H. Chavanis, Derivation of the core mass-halo mass relation of fermionic and bosonic dark matter halos from an effective thermodynamical model, *Phys. Rev. D* **100**, 123506 (2019).
- [36] H. J. de Vega, P. Salucci, and N. G. Sanchez, Observational rotation curves and density profiles versus the Thomas-Fermi

- galaxy structure theory, *Mon. Not. R. Astron. Soc.* **442**, 2717 (2014).
- [37] M. Kirejczyk, G. Müller, and P.-H. Chavanis, Self-gravitating Bose-Einstein gas with planar, cylindrical, or spherical symmetry: Density profiles and onset of condensation, *Phys. Rev. E* **105**, 034145 (2022).
- [38] M. Kirejczyk, G. Müller, and P.-H. Chavanis, *Relativistic Effects in Self-Gravitating Clusters of Fermi-Dirac Gas with Planar, Cylindrical, or Spherical Symmetry* (unpublished).
- [39] P.-H. Chavanis and C. Sire, Anomalous diffusion and collapse of self-gravitating Langevin particles in D dimensions, *Phys. Rev. E* **69**, 016116 (2004).
- [40] B. Bakhti, D. Boukari, M. Karbach, P. Maass, and G. Müller, Density profiles of a self-gravitating lattice gas in one, two, and three dimensions, *Phys. Rev. E* **97**, 042131 (2018).
- [41] L. Spitzer, The dynamics of the interstellar medium. III. Galactic distribution, *Astrophys. J.* **95**, 329 (1942).
- [42] G. L. Camm, Self-gravitating star systems, *Mon. Not. R. Astron. Soc.* **110**, 305 (1950).
- [43] G. B. Rybicki, Exact statistical mechanics of a one-dimensional self-gravitating system, *Astrophys. Space Sci.* **14**, 56 (1971).
- [44] J. Katz and M. Lecar, A note on the stability of one-dimensional self-gravitating isothermal systems, *Astrophys. Space Sci.* **68**, 495 (1980).
- [45] C. Sire and P. H. Chavanis, Thermodynamics and collapse of self-gravitating Brownian particles in D dimensions, *Phys. Rev. E* **66**, 046133 (2002).
- [46] P. H. Chavanis, Critical mass of bacterial populations and critical temperature of self-gravitating Brownian particles in two dimensions, *Physica A* **384**, 392 (2007).
- [47] S. Chandrasekhar and E. Fermi, Problems of gravitational stability in the presence of a magnetic field, *Astrophys. J.* **118**, 116 (1953).
- [48] J. S. Stodolkiewicz, On the gravitational instability of some magneto-hydrodynamical systems of astrophysical interest. Part III, *Acta Astronomica* **13**, 30 (1963).
- [49] J. Ostriker, The equilibrium of polytropic and isothermal cylinders, *Astrophys. J.* **140**, 1056 (1964).
- [50] A. M. Salzberg, Exact statistical thermodynamics of gravitational interactions in one and two dimensions, *J. Math. Phys.* **6**, 158 (1965).
- [51] J. Katz and D. Lynden-Bell, The gravothermal instability in two dimensions, *Mon. Not. R. Astron. Soc.* **184**, 709 (1978).
- [52] T. Padmanabhan, Liouville field theory and the partition function for two-dimensional Newtonian gravity, *Mon. Not. R. Astron. Soc.* **253**, 445 (1991).
- [53] J. J. Aly, Thermodynamics of a two-dimensional self-gravitating system, *Phys. Rev. E* **49**, 3771 (1994).
- [54] E. Abdalla and M. Reza Rahimi Tabar, Phase transition in a self-gravitating planar gas, *Phys. Lett. B* **440**, 339 (1998).
- [55] J. J. Aly and J. Perez, Thermodynamics of a two-dimensional unbounded self-gravitating system, *Phys. Rev. E* **60**, 5185 (1999).
- [56] P. H. Chavanis, Newtonian gravity in d dimensions, *C. R. Phys.* **7**, 331 (2006).
- [57] P. H. Chavanis, Virial theorem for rotating self-gravitating Brownian particles and two-dimensional point vortices, *Int. J. Mod. Phys. B* **26**, 1241002 (2012).
- [58] H. Poincaré, Sur l'équilibre d'une masse fluide animée d'un mouvement de rotation, *Acta Math.* **7**, 259 (1885).